FERMILAB-PUB-97-442-E

Two-body neutral final states produced in antiproton-proton annihilations at $2.911 \leqslant \sqrt{s} \leqslant 3.686$ GeV

T. A. Armstrong,[6] D. Bettoni,[2] V. Bharadwaj,[1] C. Biino,[7] G. Blanford,[4] G. Borreani,[7] D. Broemmelsiek,[4] A. Buzzo,[3] R. Calabrese,[2] A. Ceccucci,[7] R. Cester,[7] M. Church,[1] P. Dalpiaz,[2] P. F. Dalpiaz,[2] D. Dimitroyannis,[5] J. Fast,[4] A. Gianoli,[2] C. M. Ginsburg,[5] K. Gollwitzer,[4] G. Govi,[7] A. Hahn,[1] M. Hasan,[6] S. Hsueh,[1] R. Lewis,[6] E. Luppi,[2] M. Macrí,[3] A. M. Majewska,[6] M. Mandelkern,[4] F. Marchetto,[7] M. Marinelli,[3] J. Marques,[4] W. Marsh,[1] M. Martini,[2] M. Masuzawa,[5] E. Menichetti,[7] A. Migliori,[7] R. Mussa,[7] S. Palestini,[7] M. Pallavicini,[3] S. Passaggio,[3] N. Pastrone,[7] C. Patrignani,[3] J. Peoples, Jr.,[1,5] F. Petrucci,[2] M. G. Pia,[3] S. Pordes,[1] P. Rapidis,[1] R. Ray,[5,1] J. Reid,[6] G. Rinaudo,[7] B. Roccuzzo,[7] J. Rosen,[5] A. Santroni,[3] M. Sarmiento,[5] M. Savrie,[2] J. Schultz,[4] K. K. Seth,[5] A. Smith,[4] G. A. Smith,[6] M. Sozzi,[7] S. Trokenheim,[5] E. Van Drunen,[4] M. F. Weber,[4] S. Werkema,[1] Y. Zhang,[6] J. Zhao,[5] and G. Zioulas[4]

(Fermilab E760 Collaboration)

[1]*Fermi National Accelerator Laboratory, Batavia, Illinois 60510*

[2]*INFN and University of Ferrara, 44100 Ferrara, Italy*

[3]*INFN and University of Genoa, 16146 Genoa, Italy*

[4]*University of California at Irvine, Irvine, California 92717*

[5]*Northwestern University, Evanston, Illinois 60208*

[6]*Pennsylvania State University, University Park, Pennsylvania 16802*

[7]*INFN and University of Turin, 10125 Turin, Italy*

(Received 30 December 1996; revised manuscript received 25 March 1997)

We have performed an experiment in the Antiproton Accumulator at Fermilab to study two-body neutral final states formed in $\overline{pp}$ annihilations. Differential cross sections are determined in the center-of-mass energy range $2.911 < \sqrt{s} < 3.686$ GeV for the final states $\pi^0\pi^0$, $\eta\pi^0$, $\eta\eta$, $\pi^0\gamma$, and $\gamma\gamma$. The energy dependence of differential cross sections at 90° in the center of mass is studied to test the predictions of phenomenological QCD scaling hypotheses which predict power-law dependence. [S0556-2821(97)02915-9]

PACS number(s): 13.75.Cs, 14.40.Gx

I. INTRODUCTION

We report measurements of differential cross sections for the annihilation processes

$$p + \overline{p} \rightarrow \pi^0 + \pi^0, \tag{1}$$

$$p + \overline{p} \rightarrow \eta + \pi^0, \tag{2}$$

$$p + \overline{p} \rightarrow \eta + \eta, \tag{3}$$

$$p + \overline{p} \rightarrow \pi^0 + \gamma, \tag{4}$$

$$p + \overline{p} \rightarrow \gamma + \gamma, \tag{5}$$

in the center-of-mass energy range $2.911 < \sqrt{s} < 3.686$ GeV. For reactions (1), (2), and (3) we present additional data at $\sqrt{s} = 4.274$ GeV.

The data are from Fermilab experiment E760, in which high-resolution charmonium spectroscopy was performed at the Antiproton Accumulator. Circulating antiprotons interacted with protons in a hydrogen gas jet to form charmonium states that were detected in charged and neutral decay modes. The experimental neutral trigger was suitable for collecting a large and unbiased sample of data for the above reactions in the center-of-mass angular range $|\cos\theta^*| \leqslant 0.6$. These data were taken parasitically so the beam energy sampling was determined by the charmonium running. Little data have been previously obtained for these reactions. In this energy range, there are prior data only for reaction (1), obtained by R704, a charmonium experiment performed at the CERN Intersecting Storage Rings (ISR) [1]. There are no higher energy data available.

The primary motivation for the study of $\overline{pp}$ annihilations to two mesons is the discovery of heavy meson resonances that couple to NN, as predicted by potential models and by QCD [2]. By studying reactions (1), (2), and (3) we obtain the following simplifications with respect to elastic and charge exchange NN scattering: the strong diffractive amplitude present in the elastic channel is absent; there are two independent amplitudes compared to five for the elastic channel; the $J^P(I^G)$ of $\pi^0\pi^0$ and $\eta\eta$ final states must be $even^+(0^+)$, the I^G of $\eta\pi^0$ must be 1^-, and the $\pi^0\gamma$ final state must have $C-$ and $J \neq 0$. Several high statistics experiments have determined differential cross sections and analyzing powers for annihilations to $\pi^+\pi^-$ [3–5] and differential cross sections for annihilations to $\pi^0\pi^0$ [6] for $2.0 < \sqrt{s} < 2.6$ GeV. Resonances have been reported based on

TABLE I. Summary of luminosities and trigger efficiencies for the data used in the $\pi^0\pi^0$, $\pi^0\gamma$, and $\gamma\gamma$ analyses.

$\sqrt{s}$ (GeV)	$\int \mathcal{L}dt$ (nb^{-1})	$\epsilon_{\pi^0\pi^0}$	$\epsilon_{\pi^0\gamma}$	$\epsilon_{\gamma\gamma}$
2.911	53.1	0.86	0.89	0.93
2.950	197.5	0.90	0.91	0.93
2.975	423.9	0.87	0.91	0.92
2.979	165.3	0.89	0.92	0.93
2.981	392.6	0.89	0.91	0.93
2.985	200.2	0.89	0.91	0.92
2.990	513.0	0.85	0.91	0.92
2.994	308.9	0.88	0.91	0.91
3.005	171.0	0.88	0.91	0.91
3.050	53.6	0.88	0.89	0.91
3.097	384.4	0.90	0.92	0.92
3.524	4342.4	0.87		
3.526	10466.7	0.88		
3.527	1016.4		0.88	0.89
3.556	1377.4	0.87	0.88	0.89
3.591	923.8	0.88	0.89	0.90
3.595	826.8	0.85	0.86	0.87
3.613	1167.2	0.86	0.87	0.88
3.616	1048.0	0.84	0.85	0.86
3.619	575.0	0.84	0.85	0.86
3.621	1216.4	0.87	0.88	0.89
3.686	994.6	0.88	0.89	0.90
4.274	332.5	0.90		

TABLE II. Summary of luminosities and trigger efficiencies for the $\eta\pi^0$ and $\eta\eta$ analyses.

$\sqrt{s}$ (GeV)	$\int \mathcal{L}dt$ (nb^{-1})	$\epsilon_{\eta\pi^0,\eta\eta}$
2.911	49.4	0.64
2.950	189.0	0.83
2.975	423.5	0.77
2.979	152.9	0.83
2.981	393.4	0.83
2.985	201.2	0.82
2.990	512.5	0.67
2.994	310.1	0.78
3.005	172.4	0.78
3.097	591.0	0.79
3.526	9883.2	0.77
3.592[a]	1709.8	0.77
3.617[b]	3868.9	0.76
4.274	357.8	0.83

[a]The sum of stacks with energies 3.591 and 3.594 GeV.
[b]The sum of stacks with energies 3.613, 3.616, 3.619, and 3.621 GeV.

partial wave analyses of these data [7–9]. However the presence of partial wave amplitudes up to $J=4$ and the assumptions made to resolve intrinsic ambiguities cause different authors to obtain quite incompatible results. Recent work [10] offers an alternative nonresonant explanation for the pronounced oscillation in the differential cross sections and large analyzing powers observed for these reactions. In this experiment, done for the purpose of studying charmonia, the angular coverage is typically $|\cos\theta^*|\leqslant 0.6$ and we cannot contemplate an accurate partial wave analysis.

One can study these data in the context of phenomenological QCD. Exclusive hadronic reactions are intrinsically nonperturbative since all of the partons in each hadron must participate in the interaction so that each parton can assume its appropriate momentum within the final state hadrons. However, it is expected that in certain kinematic regimes, notably large angle (hard) scattering at asymptotic center-of-mass energies, there are simplifications which allow a perturbative approach to be successful.

The ''dimensional counting'' approximation [11] assumes that for exclusive scattering reactions, the scaling behavior of the physical scattering amplitude ($s\to\infty$, t/s fixed) is the same as the scaling behavior of the free-quark amplitude in the Born approximation. As applied to hadron scattering, one considers a short-distance amplitude in which a single constituent of each hadron plays an active role in the scattering. The other constituents are accommodated in the final state hadrons only when they have large components of momentum transverse to the momenta of the parent hadrons. The resulting cross section is small and falls rapidly with increas-

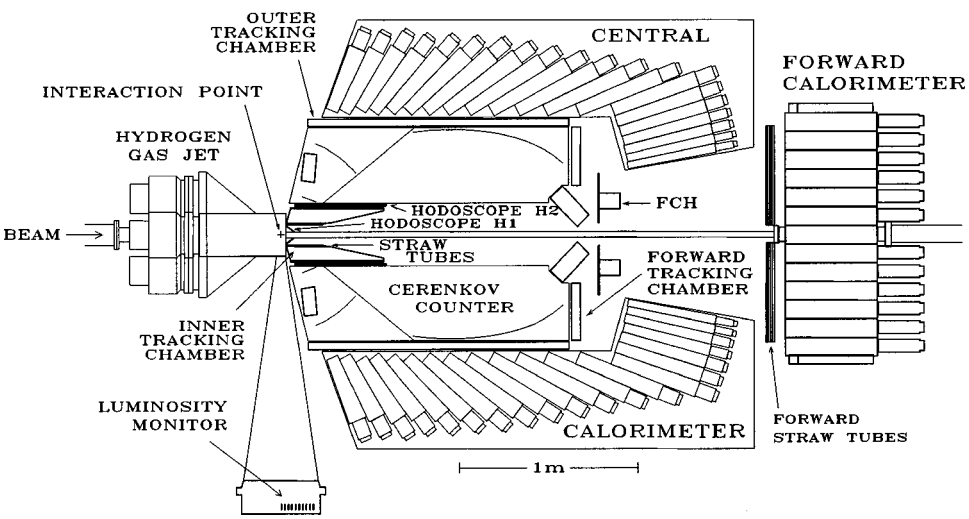

FIG. 1. E760 detector layout.

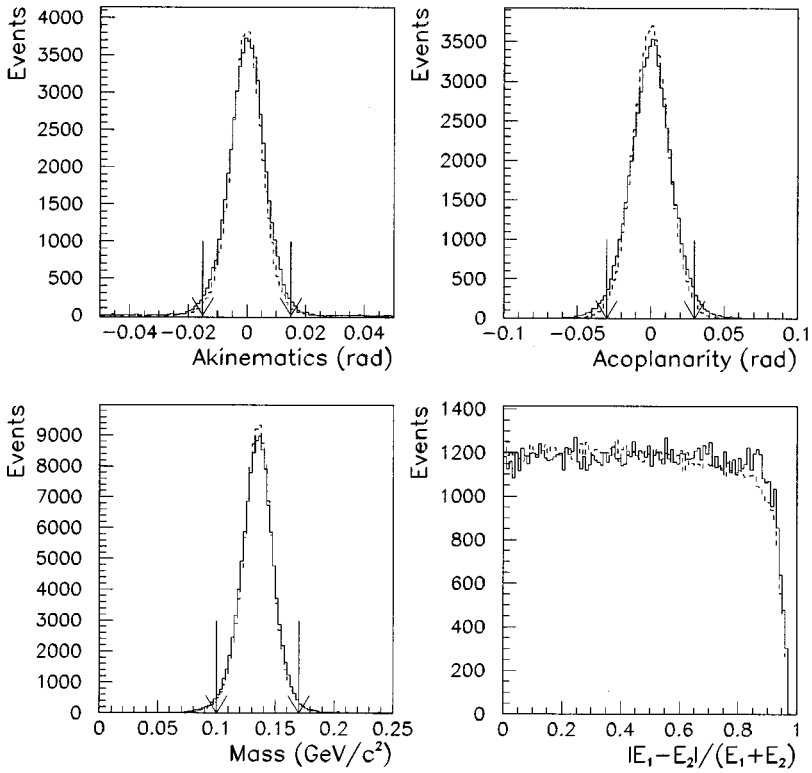

FIG. 2. Kinematical distributions for $\pi^0\pi^0$ at 2.990 GeV for all $\cos\theta^*$. The lower plots have two entries per event. E_1 and E_2 are the measured γ energies for π^0 decays. The arrows indicate cuts made for event selection.

ing s because such constituents are found comparatively rarely. The free-quark amplitude, when all of the invariants are large compared to the hadron masses, is $\sim s^{2-(n_i+n_f)/2}$, where n_i and n_f are the numbers of initial and final state partons. We then have $d\sigma/dt \sim s^{2-n_i-n_f} f(\theta)$ for the large angle differential cross section at large s. For example, pp elastic scattering is expected to fall as s^{-10} and meson proton elastic scattering as s^{-8}, in reasonable agreement with data for $\sqrt{s} \geq 8$ GeV [12]. Applying this prediction to two meson annihilations of pp, we anticipate the s dependence of $d\sigma/dt$ at fixed large angle to be s^{-8}.

An alternative model for these reactions is that of Landshoff, in which each constituent of an initial state hadron scatters on at least one constituent of the other initial state hadron such that, after scattering, the momenta of the constituents are so aligned that they recombine to make up the

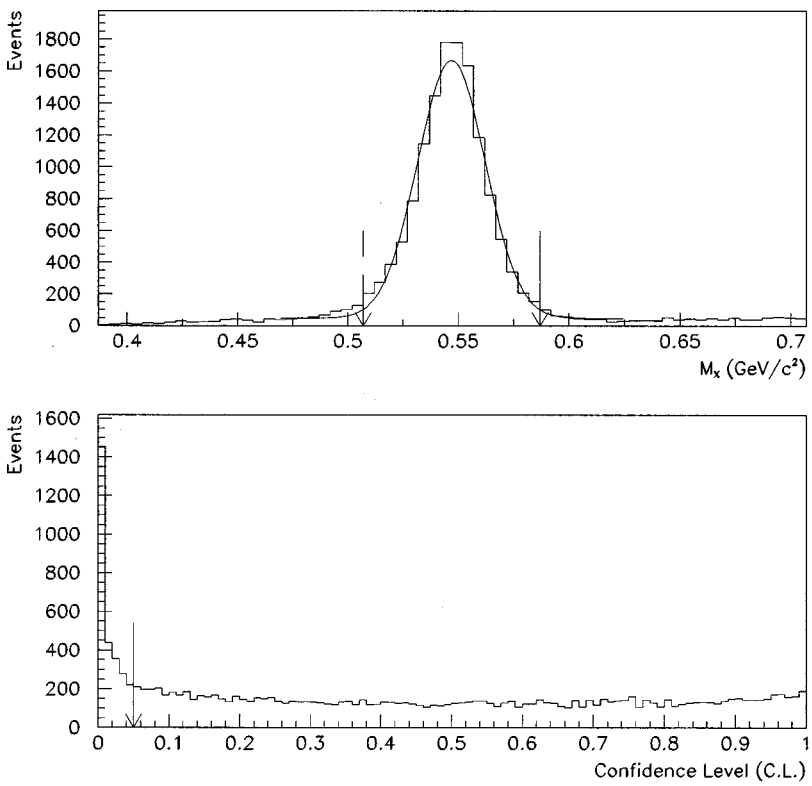

FIG. 3. M_X and confidence level for fits to $\eta\pi^0$ candidates at 2.990 GeV. The arrows indicate cuts made for event selection.

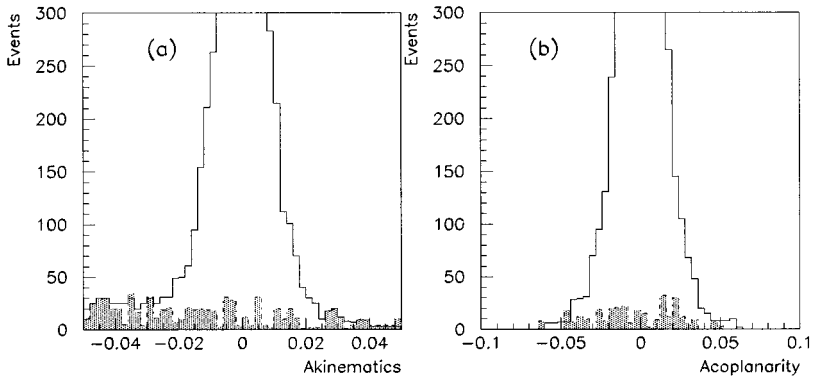

FIG. 4. *Akinematics* and *acoplanarity* distributions for $\pi^0\pi^0$ at 2.990 GeV for $\cos\theta^*<0.3$. The shaded histograms are simulated feed-down backgrounds from $\pi^0\pi^0\pi^0$ and $\pi^0\omega$.

final state hadrons [13]. The cross section is small partly because the phase space available to the constituents after they have scattered is limited, if they are to recombine. This model also gives a s^{-n} prediction for the fixed angle differential cross section, where the power depends only on the constituent-constituent differential cross sections. The predictions of the Landshoff model are in disagreement with those based on dimensional counting, giving, for example, a s^{-8} dependence of $d\sigma/dt$ for pp elastic scattering instead of s^{-10} and s^{-6} for two meson annihilations of $\overline{pp}$ instead of s^{-8}. A subsequent calculation by Mueller [14], which takes Sudakov suppression into account, modifies the predictions of this model, giving s^{-n} with n intermediate between the counting rule and Landshoff predictions, for example $s^{-9.6}$ for pp elastic scattering and $s^{-7.7}$ for $\overline{pp}$ to two mesons.

It is expected that both the short-distance amplitude and the medium-distance Landshoff amplitude will contribute to exclusive reactions [15]. The energy-dependent relative phase of these amplitudes, called the chromo-Coulomb phase shift [16], is determined by the Landshoff process and is computed in QCD. Interference between the amplitudes causes an oscillation in $\ln s$ with a period of approximately 1, which is clearly observed in the pp elastic cross section at 90° for $\ln s(\mathrm{GeV})\geqslant 2$. For $\overline{pp}$ annihilation to two mesons, we expect the period of oscillation to be roughly the same as for pp and $\overline{pp}$ elastic scattering [15]. Since the two pseudoscalar meson annihilation reactions have a slower falloff in s than these elastic scattering reactions and only two helicity amplitudes, one may observe a robust oscillation and be able to disentangle the contributing amplitudes.

In Sec. II of this paper we present the experimental technique, in Sec. III the analysis and in Sec. IV the results. We obtain the approximate power-law behavior of the 90° differential cross sections by fitting and compare our measurements with the predictions of the dimensional counting and Landshoff models. Reaction (5) was discussed in a previous publication from this experiment [17] dealing with η_c and η_c' decays to two γ's. We find no signal for this process away from the η_c and χ_2 and determine an upper limit, in disagreement with the results of CLEO [18], which measured

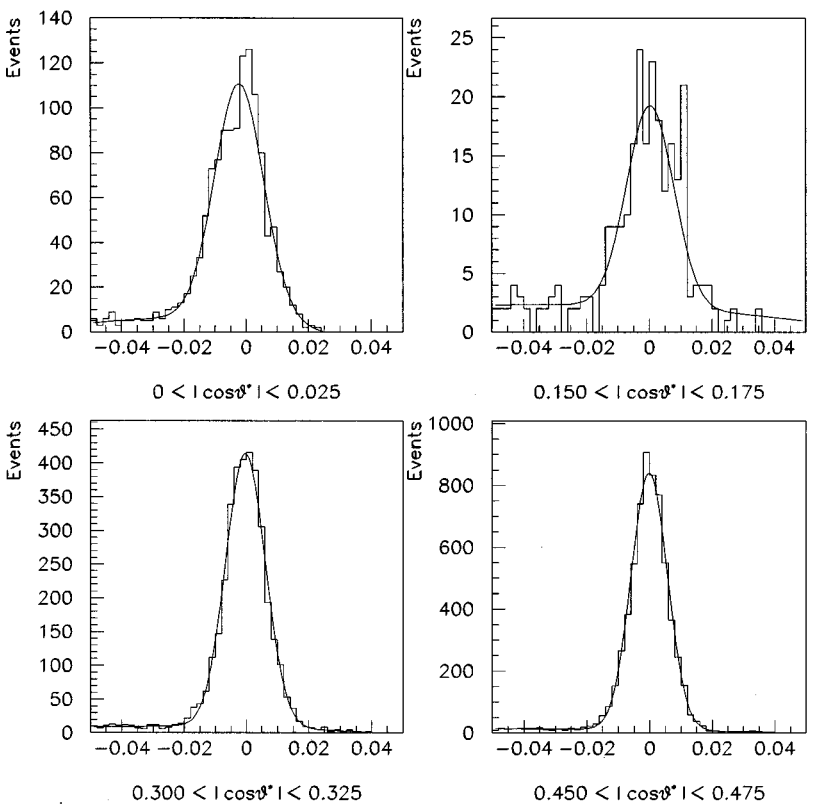

FIG. 5. *Akinematics* distributions for $\pi^0\pi^0$ in representative regions of $\cos\theta^*$ at 2.990 GeV, fit to a Gaussian plus quadratic.

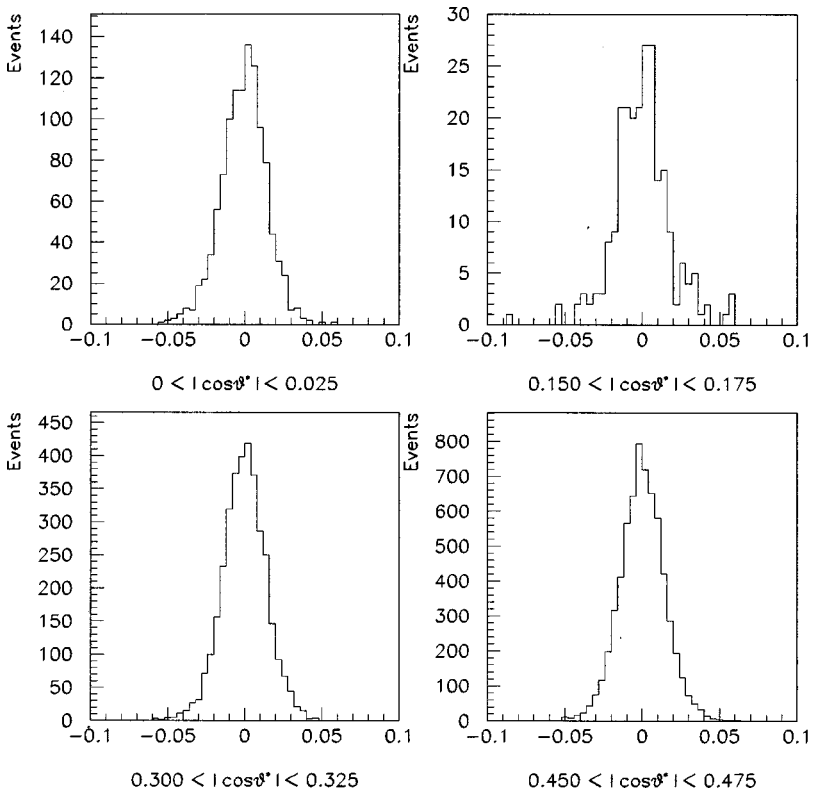

FIG. 6. *Acoplanarity* distributions for $\pi^0\pi^0$ in representative regions of $\cos\theta^*$ at 2.990 GeV.

the inverse process using virtual γ's (2 γ physics). We determine a 90% upper limit of 43 pb for the $\gamma\gamma$ reaction at 2.988 GeV with $\cos\theta^* \leqslant 0.4$, compared to the CLEO result, interpolated to the same $\sqrt{s}$, of 60 pb.

II. METHODS

A. Technique

Experiment E760 was devoted to high-resolution studies of charmonium and has been described previously [17,19]. It was carried out at the Fermilab Antiproton Source where antiprotons were stored and stochastically cooled in the accumulator ring at the design kinetic energy of 8.0 GeV. The beam was decelerated to the desired energy at which time the hydrogen gas-jet was turned on and data taking was started. Data were taken for about one beam lifetime (40 to 90 h, depending on the energy) before dumping the beam. Scans of charmonium states were performed by accumulating data at one or more energies for each ''stack.''

A total integrated luminosity of 30 pb^{-1} was collected in the center of mass energy range $2.910 \leqslant \sqrt{s} \leqslant 4.300$ GeV. Integrated luminosities for the energies at which two-body neutral final state events were analyzed are given in Tables I and II. At individual energies below 3.100 GeV integrated luminosities are typically several hundred nb^{-1}. Above 3.100 GeV, all energies but the highest (4.274 GeV) were studied with about 1 pb^{-1} or greater.

B. Experimental apparatus

Up to 5×10^{11} $\overline{p}$ were stored and cooled per stack. Both the beam and the gas jet were operated in dc mode and antiprotons crossed the $\sim 3.5\times10^{13}$ atoms/cm^2 hydrogen gas-jet target [20] with a revolution frequency of about 0.6 MHz, giving an instantaneous luminosity of up to 0.8 $\times 10^{31}$ cm^{-2} s^{-1}. The size of the interaction region was determined transversely by the beam size, $\sim$5 mm diameter, and longitudinally by the gas-jet size, $\sim$6 mm. Both figures correspond to 95% containment. For each stack we recorded the integrated luminosity and characteristics of the antiproton beam, including the revolution frequency spectrum and the orbit position, necessary to reconstruct the antiproton momentum distribution. The antiproton beam momentum resolution was $\sigma_p/p \sim 2\times10^{-4}$.

The integrated luminosity for each stack was obtained by counting the number of recoil protons from $\overline{p}p$ elastic scattering in a silicon detector located at 86.5° from the beam direction [21]. The absolute luminosity was determined using the known $\overline{p}p$ elastic scattering cross section, the solid angle subtended by the detector, and the detector efficiency. The uncertainty in integrated luminosity is approximately 4%.

The E760 detector, shown in Fig. 1, was a nonmagnetic spectrometer with cylindrical symmetry about the beam axis [19], optimized for the identification of charmonium states decaying to e^+e^-X or $\gamma\gamma$ and for multi-γ final states. It covered the entire azimuth (ϕ) and polar angle (θ) range from 2° to 70°. It consisted of three sets of scintillator hodoscopes, two in the central region (H1, H2) and one in the forward region (FCH), a multicell threshold gas Čerenkov counter for electron identification [22], several layers of charged tracking detectors, and two electromagnetic calorimeters, the forward lead-scintillator sandwich calorimeter (FCAL) [23] and the central lead glass calorimeter (CCAL) [24] covering the regions $2° \leqslant \theta \leqslant 11°$ and $11° \leqslant \theta \leqslant 70°$, respectively.

CCAL was the essential detector element for identifying neutral final states. It was designed to distinguish between

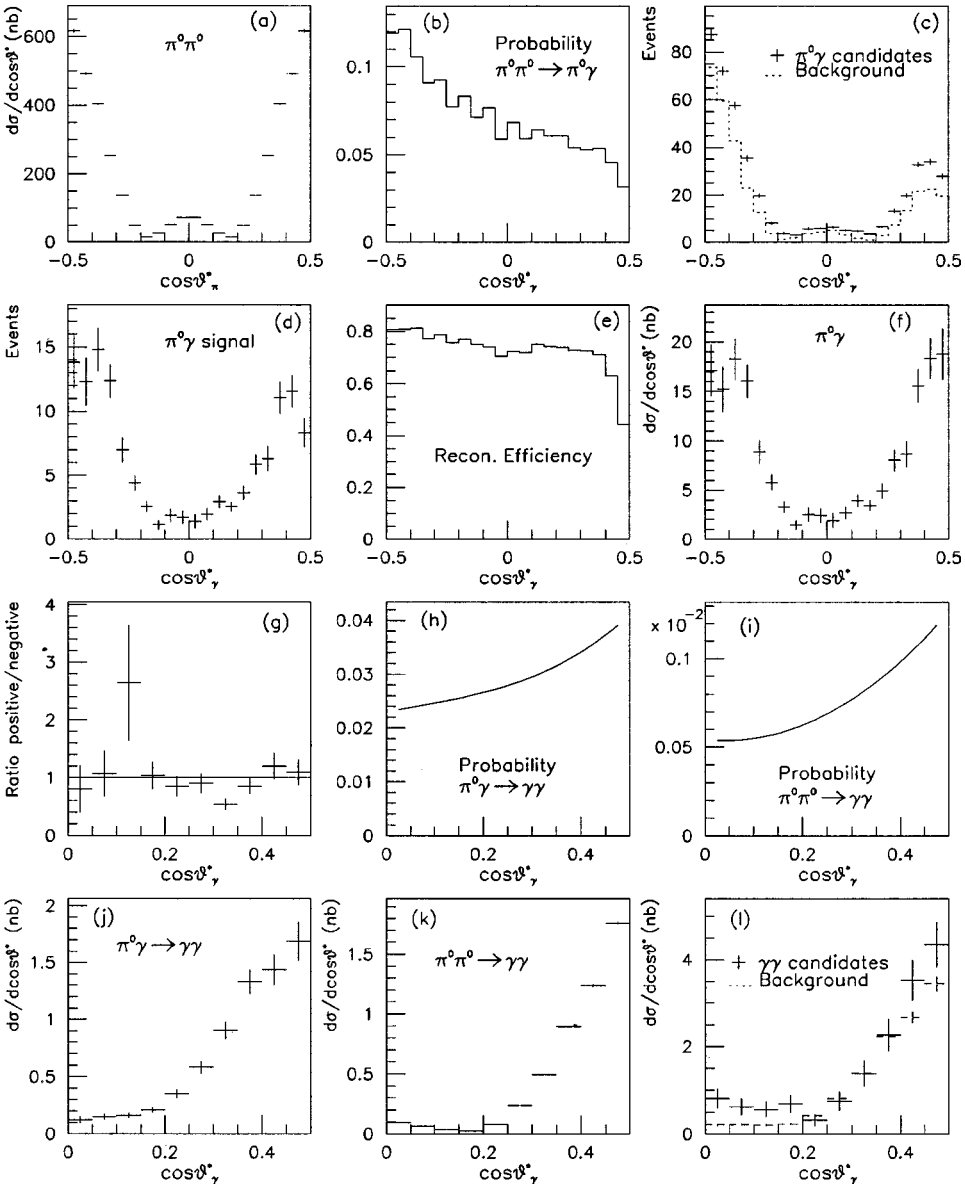

FIG. 7. Analysis of feed-down backgrounds to $\pi^0\gamma$ and $\gamma\gamma$ at 2.990 GeV. See text for description.

$\overline{p}p \to \gamma\gamma$ events and those from processes such as $\overline{p}p \to \pi^0\pi^0$ and $\overline{p}p \to \pi^0\gamma$, which have cross sections up to 10^3 times larger than those of $\overline{p}p \to \gamma\gamma$. Identifying these processes requires a granularity adequate to identify the two γ's from symmetric π^0 decays, and a low-energy threshold to detect the low-energy γ's from highly asymmetric π^0 decays.[1] The central calorimeter consisted of 1280 (64 in ϕ by 20 in θ) lead glass Čerenkov counters pointing to the beam-jet interaction region. The average rms energy resolution was $\sigma_E/E = 6.0\%/\sqrt{E(\mathrm{GeV})} + 1.4\%$ and the effective energy threshold was 20 MeV. The average rms error on the reconstructed centroid of an electromagnetic shower was 9 mm, which combined with the uncertainty in the interaction point to give an angular resolution of 6 mrad in θ and 11 mrad in ϕ. The energy calibration of these counters was obtained *in situ* using both $\overline{p}p \to \psi \to e^+e^-$ and $\overline{p}p \to \pi^0\pi^0$ events.

C. Trigger

The total $\overline{p}p$ cross section is about 70 mb in our energy region, corresponding to an interaction rate of about 700 kHz at the experiment peak luminosity of $\sim 10^{31}\ \mathrm{cm}^{-2}\ \mathrm{s}^{-1}$. Events of interest were selected by a fast hardware trigger (level one), and then transferred to a set of processors where a software filter (level two) was applied before recording the events on tape. The level-one trigger accepted in parallel (a) final states containing a large mass object decaying either into an e^+e^- pair (a1) or into two γ's (a2), (b) all neutral final states where $\geqslant$80% of the even energy was contained in the central calorimeter (ETOT), (c) a sample of events containing only two charged particles consistent with two-body kinematics, and (d) a sample of minimum bias events. The data described here comes in on the (a2) and (b) triggers.

The element common to the (a1) and (a2) triggers was the requirement (PBG1) for two energetic clusters in the central

[1]Symmetric refers to decays where the two γ's have similar energies and therefore a minimum opening angle; highly asymmetric refers to decays where one of the γ's takes almost all the energy of the parent π^0.

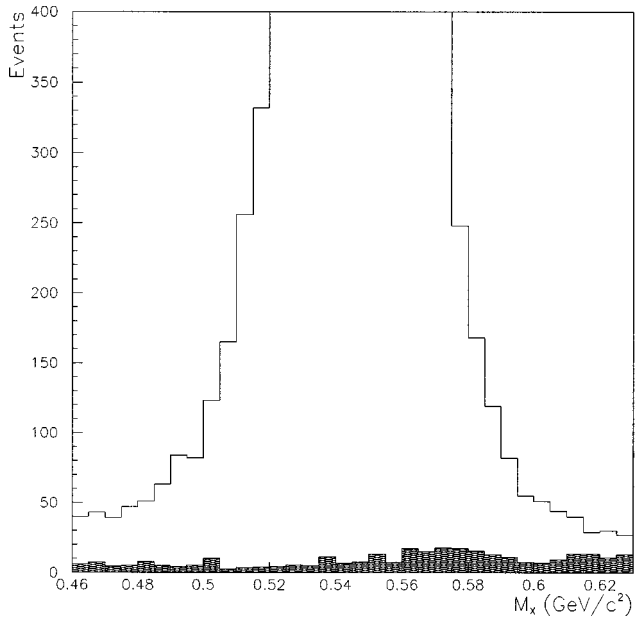

FIG. 8. M_X distribution for $\eta\pi^0$ for all cos θ^* at 2.990 GeV. The shaded distribution is simulated feed-down background from $\pi^0\pi^0\pi^0$, $\pi^0\pi^0\eta$, $\pi^0\eta\eta$, and $\pi^0\omega$.

calorimeter, topologically consistent with the kinematics of the e^+e^- and $\gamma\gamma$ final states. To select events of type (a2), we required that no charged particles be detected in the final state, a condition implemented by vetoing on signals from H1 or FCH, which together fully covered the polar angle range $2°\leqslant\theta\leqslant 65°$ over the complete azimuth. The PBG1 requirement was satisfied by a large fraction of the $\pi^0\pi^0$ and $\pi^0\gamma$ events, in which the $\pi^0\to\gamma\gamma$ decays are either reasonably symmetric or asymmetric. However, $\eta\pi^0$ and $\eta\eta$ events rarely satisfy PBG1 because of the larger opening angles of the $\eta\to\gamma\gamma$ decays. The level-one trigger rate for (a2) was $\leqslant$50 Hz. To select events of type (b) we also required that no energy be detected by FCAL (threshold approximately 100 MeV). The level-one trigger rate for (b) was $\leqslant$700 Hz. Both (a2) and (b) effectively exclude two-body final states at small polar angle.

The level-two filter was performed by 26 Fermilab ACP processors. The clustering algorithm used in the ACP was a simplified version of the one used in the offline analysis (described below). Events with a two-cluster invariant mass $\geqslant$2.0 GeV/c^2, or with the total CCAL energy $\geqslant$90% of the available energy, were written on tape. The level-two filter rejected $\sim$80% of the level-one triggers of type (b), leading to a rate to tape of $\leqslant$150 Hz.

III. ANALYSIS

We describe the reconstruction of electromagnetic showers in CCAL, identification of π^0's, event selection, determination of the efficiency of the analysis chain, and the evaluation of backgrounds. The overall efficiency is the product of the trigger efficiency, the level-two filter efficiency, and the combined efficiency, which includes the acceptance of the detector and the efficiency for selecting and reconstructing events offline.

A. Shower analysis

The algorithm for shower reconstruction in the central calorimeter is fully described in Ref. [17]. It searches for local maxima (counters with more energy than their eight nearest neighbors) and forms 3 by 3 clusters around these. Energy thresholds of 5 MeV for the central counters and 20 MeV for a nine counter region are used. The transverse co-

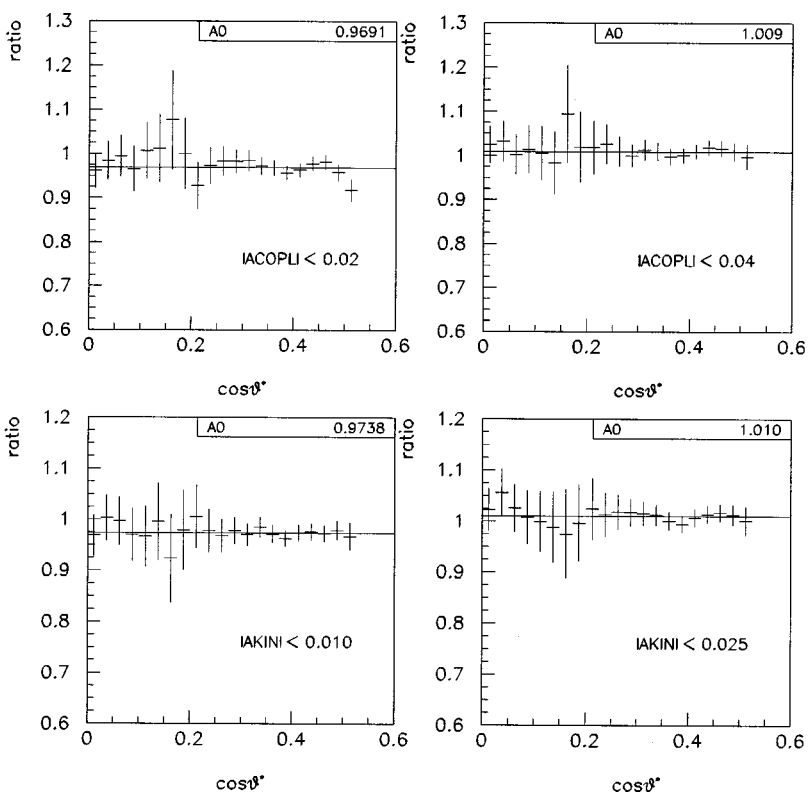

FIG. 9. $\pi^0\pi^0$ differential cross sections ratios at 2.990 GeV for test *akinematics* and *acoplanarity* cuts to the nominal cuts of 0.015 and 0.03, respectively.

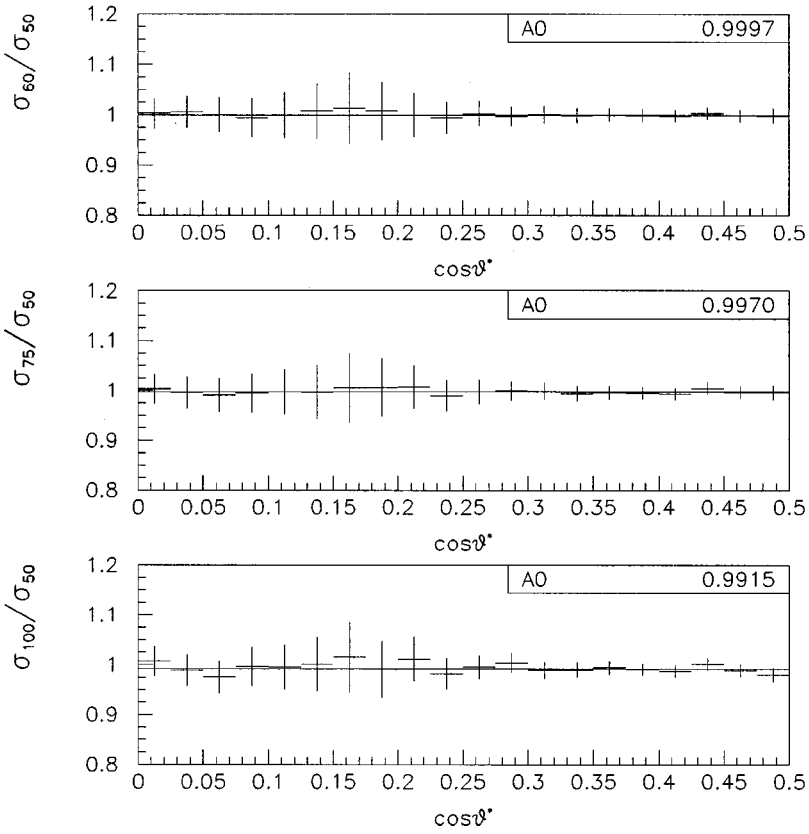

FIG. 10. $\pi^0\pi^0$ differential cross-section ratios at 2.990 GeV for test CCAL γ energy thresholds to the nominal threshold of 50 MeV.

ordinate of the cluster centroid is determined using an empirically obtained parametrization of the shower shape. When two clusters overlap, their coordinates and energies are resolved using an iterative procedure [25].

The support structure of the central calorimeter modules introduced a small amount of passive material representing 2.8% of the surface area of the detector, as seen by the incoming γ's. For a γ impinging near (or in) a crack, a significant fraction of the energy was released in the passive material and escaped detection. An empirically derived correction is applied to the energy of the shower which is a function of the γ impact point with respect to the central counter edges. At the edges the correction is as large as 45%. The variation in calorimeter response does not measurably degrade the γ trigger efficiency, which is nearly unity.

B. π^0 identification

π^0 decays which are nearly symmetric or highly asymmetric can be mistaken for single γ's. The symmetric decay of a high-energy π^0 leads to a separation between γ's which is as small as 1.5 calorimeter block widths. In order to identify such cases, an effective mass was calculated for each cluster:

$$m_{\rm cluster}=\sqrt{\left(\sum_i E_i\right)^2-\left(\sum_i \vec{p}_i\right)^2}, \qquad (6)$$

where E_i is the energy deposited in the ith counter of the cluster, $\vec{p}_i=E_i\hat{r}_i$ and $\hat{r}_i$ is the unit vector from the interaction point to the center of the ith counter. The sums are for a 5 by 5 array of counters about the cluster centroid. Clusters due to symmetric π^0 decays have large $m_{\rm cluster}$ values, and are well separated from clusters due to single γ's (or electrons) as shown by Fig. 3 of Ref. [17], where we estimate that identification of symmetric π^0 decays based on an $m_{\rm cluster}$ cut is more than 99% efficient. Any cluster with $m_{\rm cluster}\geqslant 100$ MeV/c^2 is split into 2, as described in Ref. [17], each part representing an individual γ from the π^0. There is a modest misidentification of highly asymmetric π^0 decays when a γ is outside the CCAL acceptance or its energy is below the CCAL threshold. Highly asymmetric π^0 decays in which one γ is undetected lead to ''feed-down'' backgrounds to the $\pi^0\gamma$ and $\gamma\gamma$ channels.

C. CCAL timing

When running at high instantaneous luminosities, we suffered a significant pileup rate in CCAL. For example, at 3.526 GeV with $\mathcal{L}=0.7\times10^{31}$ cm^{-2} sec^{-1}, one out of four events had at least one cluster from an out-of-time interaction, with an average of 1.5 such clusters per event. CCAL was not instrumented with time to digital convertors (TDC's). However nearly all clusters with energies above 120 MeV can be identified as ''in-time'' or ''out-of-time'' by means of a system of analog to digital converters (ADC's) with overlapping gates, described in Ref. [26]. We are frequently unable to make a timing determination for clusters with smaller energies, which are then identified as ''undetermined.'' The efficiency for timing determination falls to 85% at 20 MeV.

D. Event selection

Depending upon the channel, events are selected which pass either the PBG1(a2) trigger and/or the ETOT (b) trig-

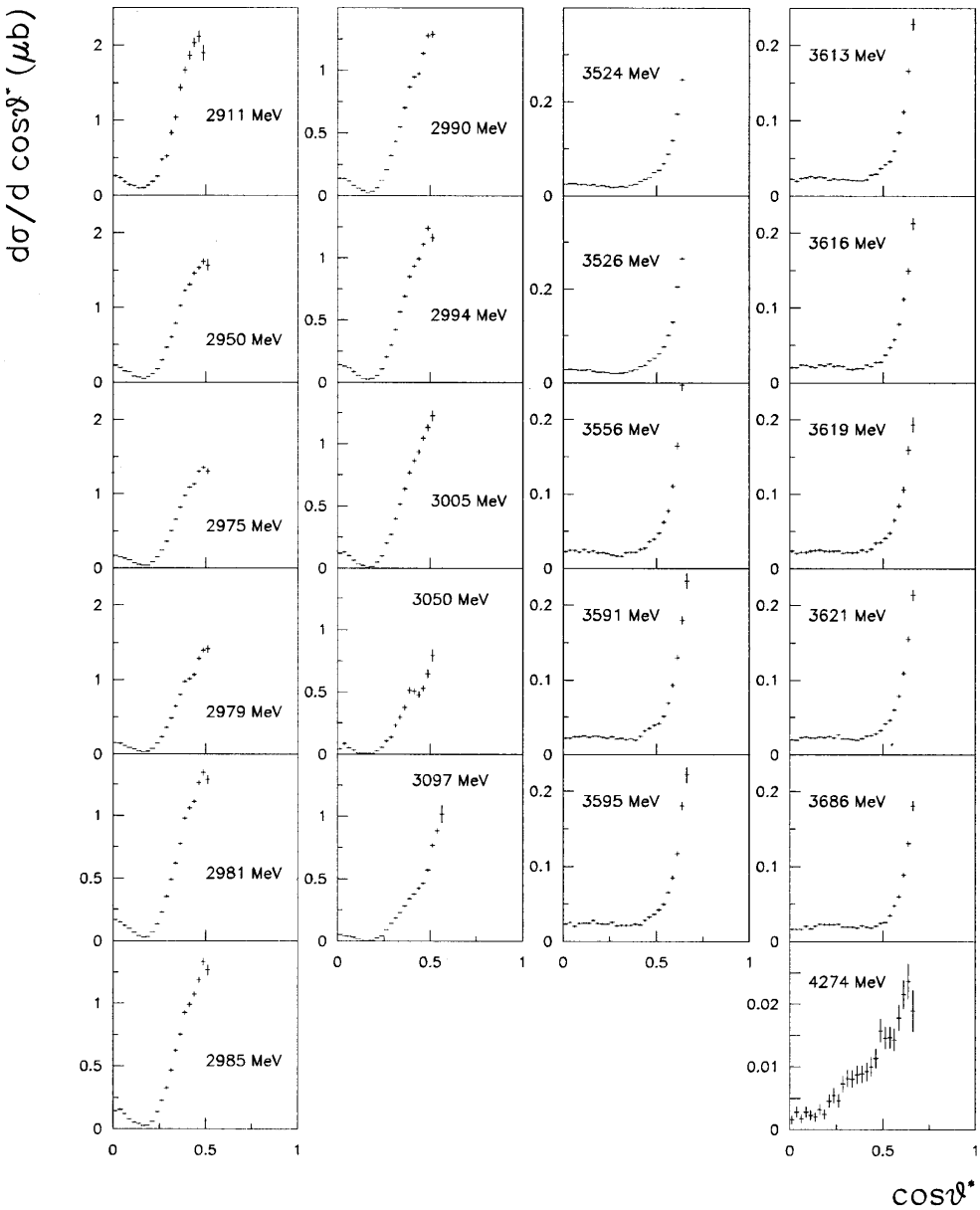

FIG. 11. $\overline{p}p \to \pi^0\pi^0$ differential cross sections in the center-of-mass energy range 2.9 to 4.3 GeV.

ger. For events passing the ETOT (b) trigger, the following additional cuts are made for all channels: The summed energy of all clusters is $\geqslant$90% of the event energy; the summed momentum parallel to the beam of all clusters is within $\pm$15% of the nominal beam momentum; the summed momentum perpendicular to the beam of all clusters is $<$350 MeV/c.

For both triggers, a fiducial cut of $11.5° < \theta_\gamma < 64.7°$ is applied to each cluster in order to reduce edge effects in CCAL.

1. $\pi^0\pi^0$

We accept candidates passing the PBG1(a2) and ETOT(b) triggers with exactly four in-time or undetermined clusters in CCAL, each with $E_{\rm cluster} \geqslant 50$ MeV. For each event, the γ's are combined in all combinations to form $\pi^0\pi^0$. The pairing associated with the smallest value of $\sqrt{(\Delta\theta)^2+(\Delta\phi)^2}$ is taken as the event topology. Here $\Delta\theta$ (*akinematics*) is the difference $\theta_1 - \theta_{1\rm comp}$, where θ_1 is the measured laboratory polar angle of the more energetic π^0 and $\theta_{1\rm comp}$ is the same quantity, computed from the measured polar angle of the other π^0 while assuming the $\pi^0\pi^0$ hypothesis and $\Delta\phi$ (*acoplanarity*) is the difference $\pi - |\phi_1 - \phi_2|$, where ϕ_1 and ϕ_2 are the measured azimuthal angles of the two π^0's.

Events are selected as $\pi^0\pi^0$ events by applying the following kinematical cuts, illustrated in Fig. 2: $|\Delta\theta| < 15$ mrad for $E_{\rm c.m.} < 3.1$ GeV and $|\Delta\theta| < 11$ mrad for $E_{\rm c.m.} > 3.1$ GeV; $|\Delta\phi| < 30$ mrad; for each γ pair identified as a π^0, 100 MeV/$c^2 < M_{\pi^0} < 170$ MeV/c^2, where M_{π^0} is computed using the cluster energies and transverse coordinates obtained as described above. If the π^0 is the result of a split cluster, the mass cut is not applied since it is assumed in the clusterization that the original cluster is a symmetric decay of an energetic π^0. Figure 2 shows the *akinematics*, *acoplanarity*, π^0 invariant mass and π^0 decay energy asymmetry for $\pi^0\pi^0$ events. Each distribution is shown after applying the cuts described above to the other kinematical distributions. The dashed lines are the predictions for these distributions from the Monte Carlo simulation of the experiment (see Sec. III G).

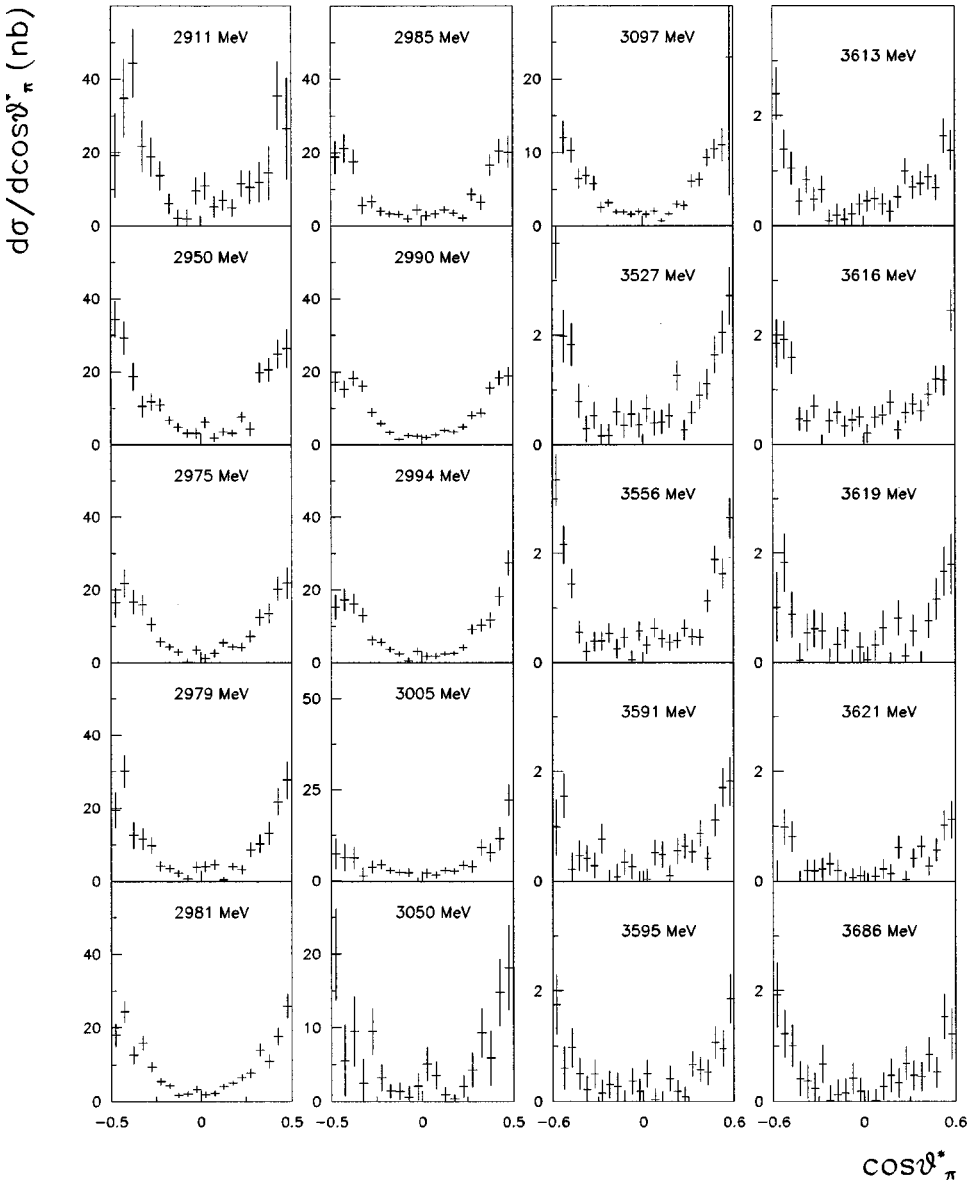

FIG. 12. $\overline{p}p \to \pi^0\gamma$ differential cross sections in the center-of-mass energy range 2.9 to 3.7 GeV.

2. $\pi^0\gamma$

We accept candidates passing the PBG1 (a2) or ETOT (b) triggers which have exactly three in-time or undetermined calorimeter clusters, each with $E_{\text{cluster}} \geqslant 50$ MeV. For each event, the γ's are combined in all combinations to form $\pi^0\gamma$. The combination associated with the smallest value of $\sqrt{(\Delta\theta)^2+(\Delta\phi)^2}$ is taken as the event topology, where $\Delta\theta$ and $\Delta\phi$ are the *akinematics* and *acoplanarity*, respectively, in analogy with the $\pi^0\pi^0$ channel. The π^0 mass cut described above is applied. A five constraint (5C) kinematic fit to the $\pi^0\gamma$ hypothesis, using the SQUAW program [27], is performed, and events with nominal confidence levels less than 10% are rejected. The nominal confidence level is computed using the expected distribution of chi squared. Since the estimated error matrix used is not accurate, we determine the fit efficiency by Monte Carlo simulation as described below.

3. $\gamma\gamma$

We accept candidates passing the PBG1(a2) trigger. Because low-energy γ's are important for rejecting backgrounds from $\pi^0\pi^0$ and $\pi^0\gamma$ events, all calorimeter clusters with energies greater than 20 MeV (compared to 50 MeV for $\pi^0\pi^0$ and $\pi^0\gamma$) are considered. We allow any number of in-time or undetermined clusters in CCAL and none in FCAL. Exactly two clusters are required to have energies greater than 100 MeV. For all cluster pairs, we require that no invariant mass falls between 80 and 200 MeV/c^2. Finally, a 4C kinematic fit to the $\gamma\gamma$ hypothesis is performed and events with nominal confidence levels less than 10% are rejected. The analysis of $\gamma\gamma$ candidates is described in greater detail in Ref. [17].

4. $\eta\pi^0$ and $\eta\eta$

For $\eta\pi^0$ and $\eta\eta$, we accept candidates passing the ETOT(b) trigger with exactly four in-time or undetermined clusters, each with $E_{\text{cluster}} \geqslant 50$ MeV, and no in-time or undetermined clusters with E_{cluster} less than 50 MeV. For each event, the clusters are combined in pairs in all possible ways.

For the $\eta\pi^0$ channel, events with one mass falling within a π^0 mass window of ± 65 MeV/c^2 and the other in an η mass window of ± 160 MeV/c^2 are selected. A five con-

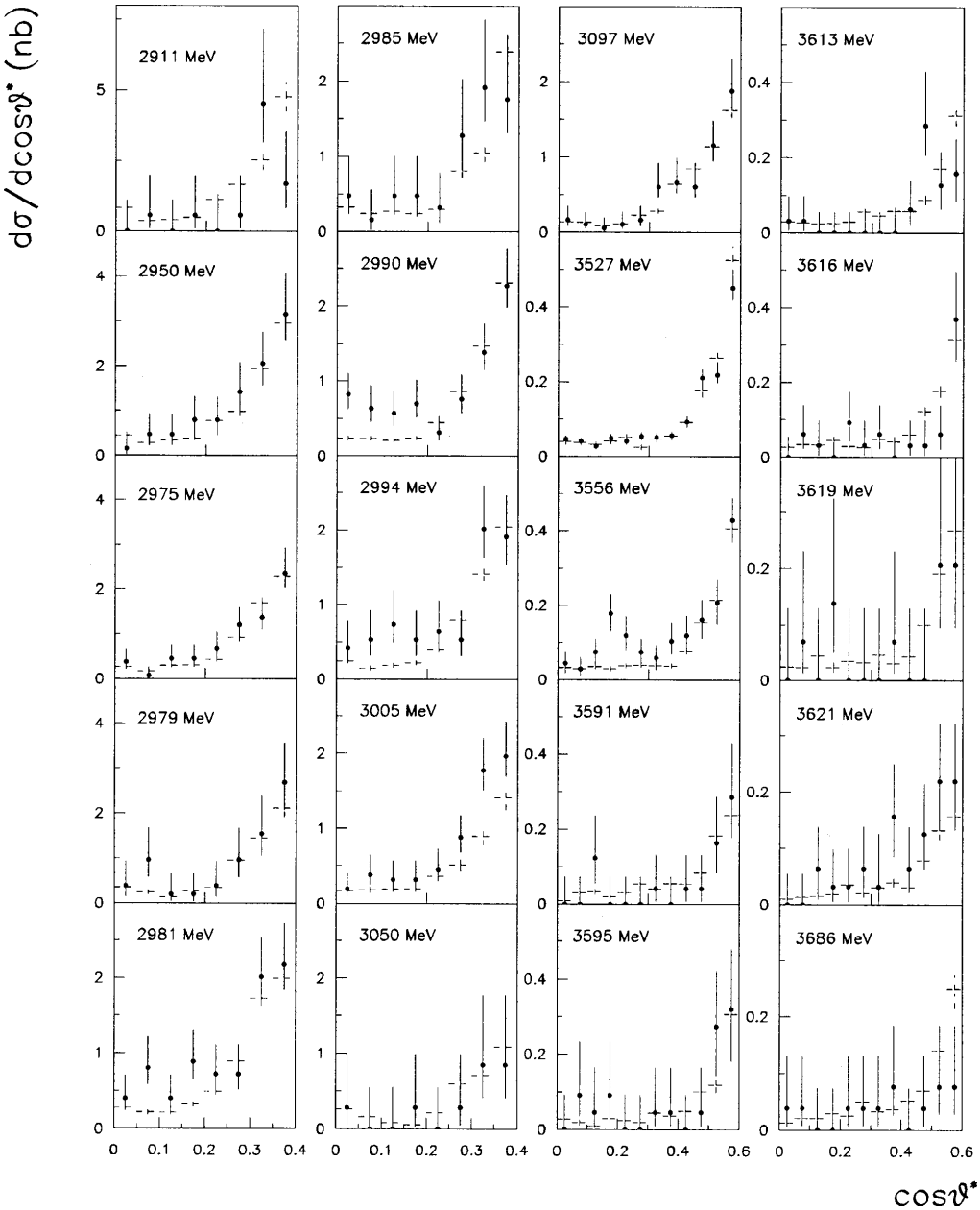

FIG. 13. Differential cross sections in the center-of-mass energy range 2.9 to 3.7 GeV for $\overline{p}p \to \gamma\gamma$ candidates (solid) and feed-down background estimates (dashed).

straint (5C) kinematical fit to the $\pi^0 X$ hypothesis is performed where M_X is unconstrained. Events with nominal confidence level less than 5% or M_X outside of a ± 40 MeV/c^2 η mass window are rejected. If more than one combination satisfies the above criteria, the one with the greater confidence level is selected. Figure 3 gives the M_X and confidence level distributions for these events.

For the $\eta\eta$ channel, candidates with both masses falling within the ± 160 MeV/c^2 η mass window are selected. A 5C kinematical fit to the ηX hypothesis is performed, where X is taken as the forward going $\gamma\gamma$ pair. Events with nominal confidence level less than 5% or M_X outside of a ± 35 MeV/c^2 η mass window are rejected. A cut is made such that events kinematically consistent with the hypothesis $\pi^0 X'$, with $M_{X'} \leqslant 1.135$ GeV/c^2 are rejected. This cut is guided by the simulation and avoids $\eta\eta$ events for which a combinatoric $\gamma\gamma$ mass, with one γ from each η decay, is fortuitously small.

E. Trigger efficiencies

We estimate trigger efficiencies for the various channels on a stack by stack basis. These include the effects of the charged particle veto for both triggers and the FCAL veto used in the ETOT(b) trigger.

1. Trigger efficiency for $\pi^0\pi^0$ and $\pi^0\gamma$

The $\pi^0\pi^0$ and $\pi^0\gamma$ events were selected by both the PBG1(a2) and the ETOT(b) triggers. The ETOT requirement was highly efficient for these channels, with an efficiency of approximately 93% at $\sqrt{s} = 2.98$ GeV, and taken to be equal for $\pi^0\pi^0$ and $\pi^0\gamma$, while the PBG1 requirement had an approximately 95% efficiency for $\pi^0\gamma$ but a lower efficiency for $\pi^0\pi^0$, about 75% at $\sqrt{s} = 2.98$ GeV, because of its topological requirement. We treat the PBG1 and ETOT requirements as uncorrelated and independent of event polar angle and determine their efficiencies for the $\pi^0\pi^0$ and $\pi^0\gamma$ channels at each stack. The PBG1(a2) and ETOT(b) trigger effi-

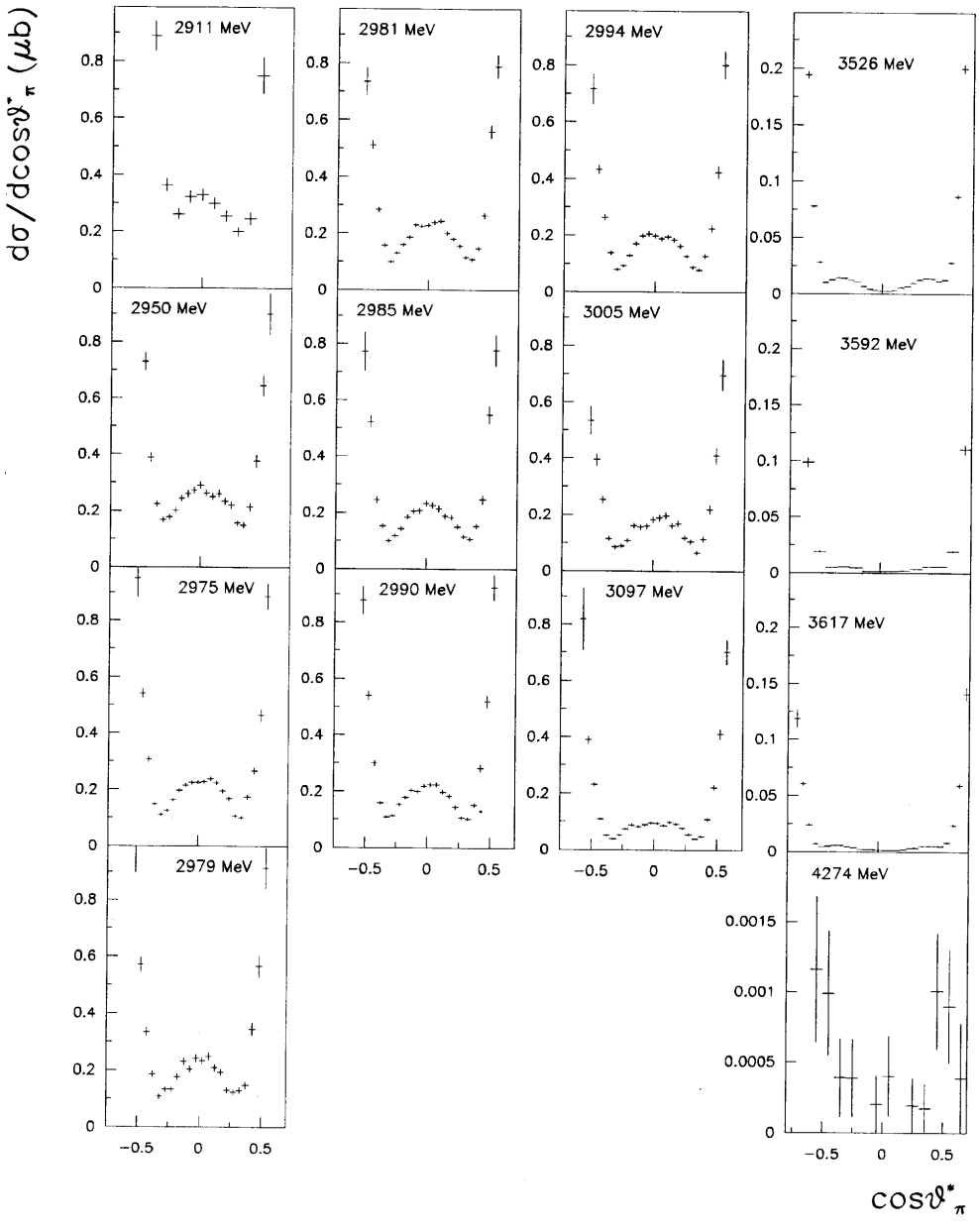

FIG. 14. $\overline{p}p \to \eta\pi^0$ differential cross sections in the center-of-mass energy range 2.9 to 4.3 GeV.

ciencies include the effects of random particles and event-associated γ conversions as discussed below.

Because of the charged particle veto, the PBG1(a2) and ETOT(b) trigger efficiencies are reduced by random charged particles and by conversions of event-associated γ's in the detector, mainly in the beam pipe. The ETOT(b) trigger efficiency is further reduced by random γ's converting in FCAL. The effect of random particles on trigger efficiencies is estimated from $\pi^0\pi^0$ data as follows: Data were taken at $\sqrt{s}=3.1$ GeV with instantaneous luminosity of 3.4×10^{30} cm^{-2} sec^{-1}, using a special trigger without an all neutral requirement and demanding only that at least 85% of the total energy was deposited in the central calorimeter. A low-background sample of $\pi^0\pi^0$ events is selected using severe kinematical cuts and mass cuts on the reconstructed pions. We are then able to measure the inefficiency introduced by the veto requirements. We find that 13.1% of the events have either the H1 or FCH trigger bit set. Subtracting the contributions from Dalitz decays (1.2% for each π^0) and γ conversions in the beam pipe (1.1% per γ), the inefficiency due to random charged particles in this special run is found to be $(13.1-2.4-4.4)\%=6.3\%$. From the fraction of events with the FCAL trigger bit set we estimate the inefficiency due to random γ's in FCAL to be 3% for this run.

The dominant source of random charged particles was δ rays produced by the antiproton beam in the target, hence this rate was luminosity and energy dependent. This dependence is studied [26] by measuring the rate of extra hits in H1 and FCH in $\overline{p}p \to \psi \to e^+e^-$, $\overline{p}p \to \chi_{1,2} \to \psi + \gamma \to e^+e^- + \gamma$, and $\overline{p}p \to \psi' \to e^+e^-$ events from data samples taken at different instantaneous luminosities. The random charged particle rate is found to increase linearly with event rate and the fit to these data is used to scale appropriately the inefficiency determined from the $\pi^0\pi^0$ data sample as described above. Inefficiencies due to random charged particles in H1 and FCH, random γ's in FCAL and event-associated γ conversions are included in the trigger efficiencies on a stack by stack basis. The overall trigger efficiencies are given in Table I.

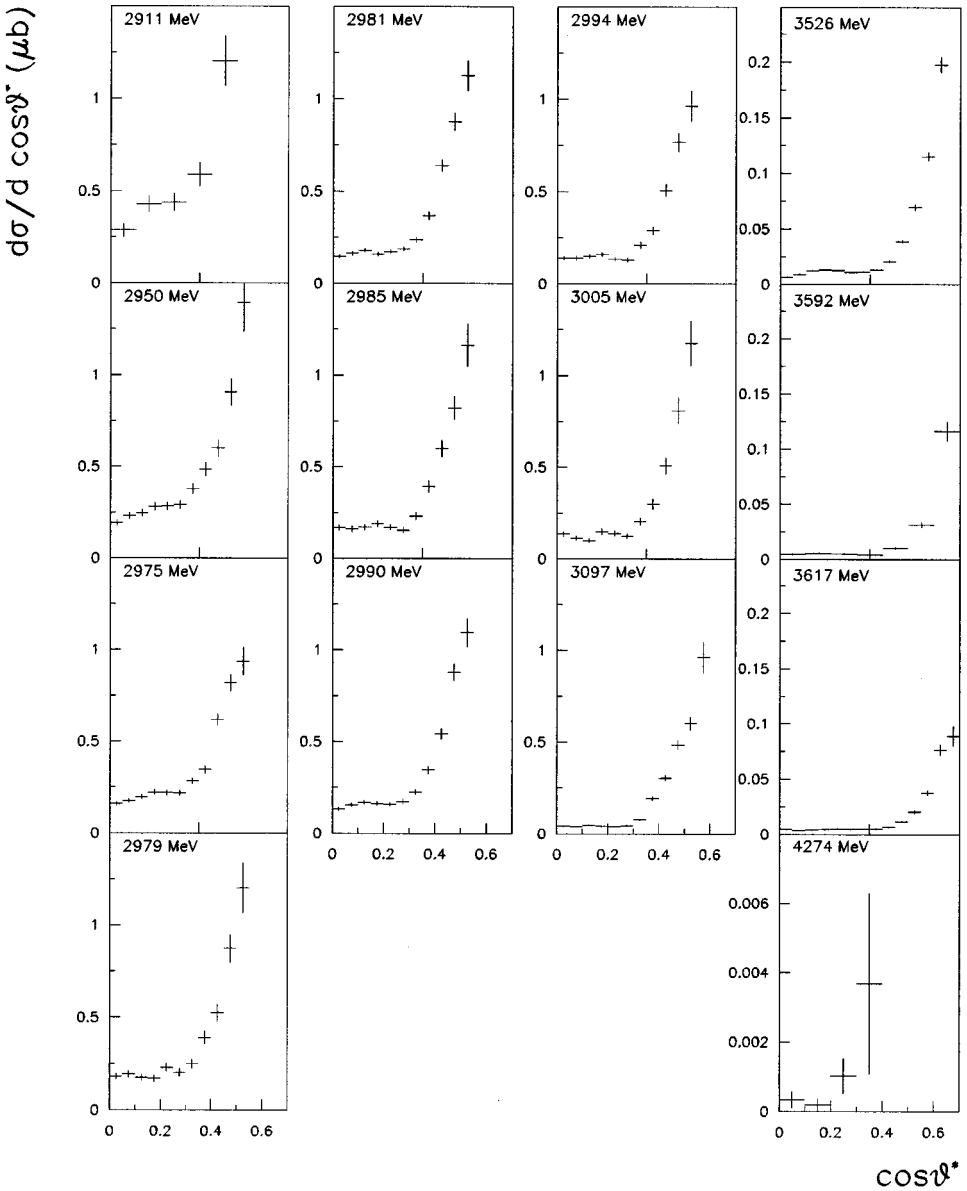

FIG. 15. $\overline{pp} \to \eta\eta$ differential cross sections in the center-of-mass energy range 2.9 to 3.7 GeV.

2. Trigger efficiency for $\gamma\gamma$

Only $\gamma\gamma$ events selected by the PBG1 trigger are used in the analysis. The PBG1 requirement was fully efficient for γ events as described elsewhere [17]. $\gamma\gamma$ trigger efficiencies including the effects of random charged particles and γ conversions are given in Table I.

3. Trigger efficiency for $\eta\pi^0$ and $\eta\eta$

These events did not normally satisfy the PBG1 trigger. Therefore, we use only events that passed the ETOT(b) trigger. For the efficiency of the ETOT requirement, we use the values determined from the $\pi^0\pi^0$ data. $\eta\pi^0$ and $\eta\eta$ trigger efficiencies including the effects of random particles and γ conversions are given in Table II.

F. Filter efficiency

For each channel we require a specific number of on-time and undetermined CCAL clusters as discussed above. The efficiency of this requirement is reduced by extra CCAL clusters from unrelated events and is thus dependent upon energy and luminosity. We estimate this efficiency by studying the $\pi^0\pi^0$ data on a stack by stack basis. We select events which pass the ETOT(b) trigger using only the kinematical criteria described above and find the filter efficiency to be in the range 90–96% for all stacks. For the $\pi^0\pi^0$ and $\pi^0\gamma$ channels, we use the stack-independent value of 93 ± 3 %. Because of the more stringent extra-cluster requirement applied to the $\eta\pi^0$ and $\eta\eta$ channels, the filter efficiency is reduced and is determined to be 83 ± 3 %.

G. Monte Carlo simulation

A Monte Carlo simulation of the neutral channels was developed to obtain the geometrical acceptance of the detector, to evaluate the reconstruction efficiency of the selection and fitting algorithms, and to estimate the ''feed-down'' backgrounds, where loss of one or more γ's causes events to be shifted into channels of smaller γ multiplicity, for example, $\pi^0\pi^0$ as $\pi^0\gamma$.

For each channel we simulate events uniformly in $\cos\theta^*$, where θ^* is the center-of-mass angle. The annihila-

TABLE III. $\pi^0\pi^0$ differential cross section $d\sigma/d\cos\theta^*$(nb) for 2911 MeV$\leqslant\sqrt{s}\leqslant$2994 MeV.

$\cos\theta^*$	2911 MeV	2950 MeV	2975 MeV	2979 MeV	2981 MeV	2985 MeV	2990 MeV	2994 MeV
0.0125	262.48± 18.61	225.17± 8.76	172.11± 5.31	149.72± 7.40	167.49± 5.65	144.95± 6.89	140.51± 4.27	139.55± 5.46
0.0375	240.52± 16.48	194.89± 8.07	148.17± 4.85	147.35± 7.69	150.99± 5.44	154.17± 7.37	136.77± 4.38	129.83± 5.39
0.0625	186.43± 14.43	150.23± 6.85	129.85± 4.54	114.60± 6.64	122.40± 4.67	120.04± 6.25	117.11± 3.99	112.99± 5.07
0.0875	140.74± 12.96	136.60± 6.71	103.82± 3.98	88.20± 5.49	97.53± 4.12	80.14± 4.89	80.64± 3.18	84.66± 4.13
0.1125	131.70± 12.18	80.37± 4.84	67.34± 3.17	68.76± 4.99	66.85± 3.47	52.68± 3.90	59.93± 2.72	55.51± 3.33
0.1375	102.38± 10.19	71.20± 4.52	50.08± 2.68	42.24± 3.70	40.61± 2.61	42.32± 3.49	40.19± 2.20	28.78± 2.25
0.1625	102.96± 10.00	49.88± 3.54	34.89± 2.19	30.10± 3.04	29.52± 2.08	26.21± 2.53	20.71± 1.45	25.06± 2.11
0.1875	135.32± 12.46	72.26± 4.53	40.07± 2.31	37.18± 3.33	33.16± 2.14	31.48± 2.79	31.97± 1.85	32.94± 2.38
0.2125	187.29± 14.54	111.08± 5.74	79.53± 3.38	77.30± 5.18	71.45± 3.42	61.18± 4.18	64.01± 2.81	58.06± 3.35
0.2375	254.03± 16.61	172.77± 7.04	149.22± 4.77	142.61± 7.12	133.94± 4.78	137.05± 6.43	123.90± 3.96	107.16± 4.62
0.2625	481.14± 24.15	293.30± 9.30	238.54± 5.96	230.68± 9.10	228.63± 6.23	226.95± 8.44	207.40± 5.14	203.04± 6.48
0.2875	525.95± 25.13	463.10±12.06	360.85± 7.34	359.37± 11.35	354.74± 7.88	325.05± 9.95	321.41± 6.33	296.14± 7.64
0.3125	838.84± 31.86	604.53±13.79	500.44± 8.83	485.18± 13.60	489.14± 9.48	466.64± 12.15	432.05± 7.49	421.49± 9.41
0.3375	1035.52± 35.15	787.60±15.75	654.99± 9.96	643.04± 15.44	621.29± 10.58	621.95± 14.22	545.99± 8.40	564.29± 10.92
0.3625	1435.23± 43.79	1023.72±18.37	817.64±11.30	796.47± 17.29	774.10± 11.76	752.67± 15.47	700.25± 9.50	690.83± 12.13
0.3875	1667.79± 47.75	1226.85±20.81	977.88±12.73	977.87± 20.08	977.09± 13.88	925.67± 17.88	866.98± 10.99	848.53± 13.89
0.4125	1864.32± 52.94	1311.65±21.75	1089.53±13.79	1014.17± 20.80	1059.71± 14.60	989.42± 18.95	945.52± 11.72	934.08± 14.94
0.4375	2034.90± 60.75	1459.26±24.27	1131.32±14.36	1067.47± 21.84	1111.99± 15.46	1072.81± 20.27	973.21± 12.16	993.25± 15.71
0.4625	2113.91± 75.31	1532.84±28.80	1303.57±17.49	1285.92± 27.19	1260.93± 18.34	1188.49± 23.56	1134.76± 14.51	1108.17± 18.23
0.4875	1897.16± 102.29	1616.50±37.81	1353.97±21.95	1397.69± 35.10	1342.39± 23.28	1333.10± 30.54	1274.57± 18.87	1237.84± 23.34
0.5125			1302.54±35.39	1414.55± 54.81	1286.67± 35.10	1267.93± 44.31	1287.62± 27.53	1163.08± 32.10

tion points are chosen in the interaction region with a distribution based on the shapes of the beam and gas-jet target. γ's from π^0 and η decays are generated and propagated to CCAL and FCAL. $\omega\rightarrow\pi^0\gamma$ decays in channels simulated to study backgrounds are assumed to be isotropic. γ interactions in CCAL are simulated based on the parametrization of the transverse energy distribution which we use in the offline analysis to model electromagnetic showers. The energies deposited in the blocks and cracks are allowed to fluctuate so that the experimental energy resolution of CCAL is obtained. The energy deposit for each block is converted to analog to digital converter (ADC) counts to which a simulated pedestal fluctuation is added. The simulated events are subjected to the same analysis as the data. For each channel and energy, the resulting binned angular distribution represents the combined efficiency which includes the acceptance of the detector and efficiency for selecting and reconstructing events. The Monte Carlo simulation is in good agreement with our data, as shown below and in related analyses [17,28]

H. Geometrical acceptance and reconstruction efficiency

The experimental angular distributions must be corrected for the combined efficiency estimated above. Because the

TABLE IV. $\pi^0\pi^0$ differential cross section $d\sigma/d\cos\theta^*$(nb) for 3005 MeV$\leqslant\sqrt{s}\leqslant$3595 MeV.

$\cos\theta^*$	3005 MeV	3050 MeV	3097 MeV	3524 MeV	3526 MeV	3556 MeV	3591 MeV	3595 MeV
0.0125	118.81± 6.77	42.89± 6.06	54.09± 3.04	24.79±0.50	27.35±0.55	22.50± 1.33	21.84± 1.25	23.47± 1.34
0.0375	131.63± 7.40	87.51±10.61	42.86± 2.60	25.86±0.48	28.46±0.53	24.55± 1.48	21.69± 1.32	25.41± 1.48
0.0625	99.60± 6.18	53.67± 7.17	36.76± 2.43	25.79±0.49	27.51±0.53	24.14± 1.47	23.76± 1.40	20.03± 1.34
0.0875	62.15± 4.57	34.65± 5.48	28.74± 2.14	23.84±0.50	26.48±0.54	21.82± 1.33	23.96± 1.37	23.88± 1.42
0.1125	32.22± 2.87	12.85± 2.87	18.33± 1.60	24.63±0.47	25.88±0.50	25.42± 1.47	25.04± 1.38	24.54± 1.43
0.1375	22.04± 2.45	7.48± 1.76	4.29± 0.58	22.78±0.43	27.13±0.50	22.02± 1.40	23.43± 1.38	24.27± 1.46
0.1625	8.30± 1.10	5.98± 2.12	3.97± 0.60	24.07±0.47	24.14±0.49	23.52± 1.45	24.45± 1.39	27.86± 1.57
0.1875	15.77± 1.94	6.38± 2.60	8.00± 0.92	21.08±0.45	23.38±0.48	20.93± 1.31	24.31± 1.37	23.78± 1.41
0.2125	46.71± 3.74	26.84± 4.82	25.52± 1.89	22.17±0.42	22.74±0.45	21.16± 1.32	23.39± 1.32	23.19± 1.37
0.2375	96.09± 5.76	58.18± 7.33	41.38± 2.36	19.75±0.39	21.63±0.43	19.84± 1.31	21.96± 1.31	23.25± 1.41
0.2625	202.14± 8.81	107.38±10.06	90.67± 3.85	17.92±0.38	20.33±0.42	17.90± 1.21	23.83± 1.35	25.46± 1.48
0.2875	271.01± 9.84	137.16±11.63	143.08± 4.81	18.75±0.40	20.41±0.45	16.96± 1.12	21.00± 1.21	20.79± 1.28
0.3125	397.38± 12.38	233.43±15.46	185.72± 5.38	19.82±0.41	21.34±0.44	16.41± 1.13	21.78± 1.23	21.10± 1.27
0.3375	512.76± 14.10	297.59±18.28	229.83± 5.99	18.79±0.39	21.98±0.45	21.39± 1.33	20.24± 1.24	21.07± 1.33
0.3625	636.28± 15.77	374.42±20.40	282.20± 6.83	22.62±0.49	24.54±0.53	21.67± 1.32	21.09± 1.23	21.56± 1.33
0.3875	766.29± 17.48	513.77±24.63	339.67± 7.51	24.95±0.54	26.80±0.58	21.98± 1.29	19.33± 1.13	22.98± 1.30
0.4125	863.65± 19.29	505.10±25.13	378.08± 7.98	30.94±0.62	33.81±0.68	25.97± 1.46	24.62± 1.35	22.01± 1.32
0.4375	934.48± 20.42	477.79±24.54	424.89± 8.67	36.25±0.76	37.24±0.79	27.42± 1.50	31.95± 1.54	28.19± 1.52
0.4625	1042.69± 23.26	528.94±26.38	464.32± 9.29	40.07±0.86	46.30±0.97	36.32± 1.66	35.30± 1.55	32.53± 1.58
0.4875	1127.80± 29.09	645.03±33.49	570.94±10.98	50.36±0.97	52.35±1.05	39.35± 1.83	39.47± 1.66	36.21± 1.69
0.5125	1222.92± 41.34	793.88±46.94	766.99±15.24	55.18±1.14	62.39±1.28	47.81± 2.00	41.59± 1.74	42.27± 1.86
0.5375			882.73±21.92	68.75±1.39	76.69±1.56	62.30± 2.28	51.37± 1.89	49.68± 1.96
0.5625				88.79±1.58	101.60±1.82	77.13± 2.66	68.77± 2.31	65.54± 2.35
0.5875				118.08±2.03	129.12±2.21	110.37± 3.32	92.95± 2.78	84.94± 2.79
0.6125				174.09±2.19	204.94±2.45	164.49± 4.54	129.89± 3.47	117.05± 3.46
0.6375				247.08±1.58	265.10±1.73	245.61± 7.41	180.27± 5.15	180.75± 5.45

TABLE V. $\pi^0\pi^0$ differential cross section $d\sigma/d\cos\theta^*$(nb) for 3613 MeV$\leq\sqrt{s}\leq$4274 MeV.

$\cos\theta^*$	3613 MeV	3616 MeV	3619 MeV	3621 MeV	3686 MeV	4274 MeV
0.0125	22.76±1.17	19.87±1.16	23.59± 1.77	20.37±1.06	16.65±1.21	1.51±0.62
0.0375	19.90±1.11	19.73±1.18	20.48± 1.63	19.73±1.06	16.48±1.19	2.74±0.83
0.0625	23.97±1.28	23.46±1.32	22.21± 1.68	23.33±1.21	16.49±1.18	1.71±0.65
0.0875	24.22±1.24	23.25±1.30	21.87± 1.69	24.07±1.19	20.46±1.36	2.72±0.82
0.1125	26.26±1.27	21.24±1.19	23.70± 1.73	22.71±1.15	17.03±1.23	2.23±0.74
0.1375	24.53±1.25	20.22±1.18	24.56± 1.76	22.38±1.14	20.74±1.31	1.98±0.70
0.1625	25.33±1.27	23.90±1.31	24.88± 1.83	23.77±1.20	23.40±1.41	3.10±0.86
0.1875	24.08±1.20	22.64±1.25	23.50± 1.73	23.08±1.18	22.80±1.45	2.37±0.75
0.2125	21.41±1.11	24.83±1.27	23.29± 1.68	24.51±1.17	22.89±1.38	4.42±1.01
0.2375	23.23±1.20	21.62±1.22	23.59± 1.73	22.74±1.17	22.76±1.36	5.25±1.12
0.2625	21.87±1.15	22.63±1.24	24.00± 1.75	27.04±1.27	23.34±1.41	4.49±1.03
0.2875	22.77±1.16	22.13±1.21	20.95± 1.59	21.63±1.11	19.56±1.30	7.01±1.26
0.3125	21.73±1.10	18.36±1.07	21.89± 1.59	21.43±1.07	19.30±1.25	7.85±1.35
0.3375	20.95±1.13	17.59±1.07	21.18± 1.63	20.39±1.08	19.69±1.24	7.78±1.35
0.3625	20.78±1.12	18.63±1.10	21.93± 1.64	19.73±1.06	18.49±1.24	8.41±1.40
0.3875	20.46±1.06	18.55±1.05	25.00± 1.69	21.93±1.08	21.07±1.32	8.52±1.35
0.4125	21.81±1.12	23.81±1.23	22.93± 1.65	25.30±1.18	19.58±1.22	8.90±1.43
0.4375	28.40±1.31	21.77±1.18	26.22± 1.80	26.01±1.22	18.00±1.18	9.66±1.49
0.4625	29.59±1.31	27.04±1.30	34.17± 2.02	28.24±1.23	20.81±1.29	10.94±1.49
0.4875	36.59±1.45	27.72±1.30	34.97± 2.04	32.34±1.31	24.30±1.38	15.23±1.81
0.5125	42.19±1.60	36.82±1.54	40.95± 2.28	41.50±1.55	25.68±1.39	14.12±1.78
0.5375	46.03±1.62	46.95±1.73	47.75± 2.39	46.44±1.61	34.78±1.71	14.18±1.71
0.5625	60.09±1.89	57.33±1.95	65.12± 2.86	59.95±1.86	47.74±1.96	13.81±1.74
0.5875	84.27±2.40	78.09±2.40	84.32± 3.43	78.72±2.23	59.80±2.30	17.20±2.01
0.6125	111.30±2.84	111.28±2.99	106.29± 4.01	109.35±2.73	88.88±3.02	20.82±2.20
0.6375	165.65±4.23	149.25±4.22	159.21± 5.95	155.16±3.93	130.39±4.07	22.84±2.71
0.6625	227.43±8.16	212.49±7.89	193.04±10.17	213.72±7.16	180.87±6.51	18.26±3.23

angular distribution is rapidly varying, correction by a binned efficiency based on a uniform distribution leads to distortion. A better correction is based on a shape similar to the actual angular distribution. We apply an iterative procedure in which we update the angular distribution used to obtain the simulated combined efficiency until the corrected angular distribution converges. We first correct the data using the simulated combined efficiency based on a uniform angular distribution. The resulting distribution is fit to a six order polynomial. The resulting function is used to weight the angular distribution used in the simulation. The procedure is repeated until the corrected angular distribution does not change. Convergence is typically obtained within three iterations. As the edges of the detector are approached the combined efficiency decreases. For each channel and energy we choose minimum and maximum $\cos\theta^*$ for which the differential cross section can be reasonably determined as those points at which the combined efficiency falls by 20%. The absolute value of the $\cos\theta^*$ cutoffs are in the range 0.45 to 0.7.

For the $\gamma\gamma$ channel, the combined efficiency is uniform from $\cos\theta^*=0$ to an energy-dependent maximum $\cos\theta^*$. These efficiencies are 0.68 ± 0.01 for $\sqrt{s}<3.1$ GeV, and 0.61 ± 0.03 for $\sqrt{s}>3.1$ GeV. They are determined from background-free samples of $\overline{p}p\to\psi\to e^+e^-$ and $\overline{p}p\to\psi'\to e^+e^-$ selected using only the hodoscopes and the Cerenkov counter [17].

I. Backgrounds

1. $\pi^0\pi^0$

In order to determine the background to the $\pi^0\pi^0$ channel, we study annihilations into higher multiplicity channels by Monte Carlo simulation based on our experimental analysis of the most important of these channels [29,30]. We find significant contributions from the $\overline{p}p\to3\pi^0$ and $\overline{p}p\to\pi^0\omega\to\pi^0\pi^0\gamma$ channels, in which a π^0 or a γ is undetected, respectively. *Akinematics* and *acoplanarity* distributions for data with $\cos\theta^*\leq0.3$ and simulated background events are given in Fig. 4 for $E_{\rm c.m.}=2.990$ GeV. In this angular regime, the simulation accurately matches the small and slowly varying background observed in the $\pi^0\pi^0$ data. For larger $\cos\theta^*$, the simulation accounts for a smaller fraction (about 60%) of the observed background, which we attribute to uncertainties in the cross sections used in the simulation.

Figures 5 and 6 are (unsubtracted) *akinematics* and *acoplanarity* plots for four different $\cos\theta^*$ intervals at $E_{\rm c.m.}=2.990$ GeV. The background to $\pi^0\pi^0$ is approximately isotropic and is typically 5% at all energies with the exception of low cross-section bins in which it becomes as large as 10%. For each $E_{\rm c.m.}$ and angular interval of size $\Delta\cos\theta^*=0.025$, the $\pi^0\pi^0$ *akinematics* distribution is fit to a Gaussian representing signal plus a quadratic representing background. Background is subtracted from each bin in the

TABLE VI. $\pi^0\gamma$ differential cross section $d\sigma/d\cos\theta^*$(nb) for 2911 MeV$\leq\sqrt{s}\leq$2994 MeV.

$\cos\theta^*_\pi$	2911 MeV	2950 MeV	2975 MeV	2979 MeV	2981 MeV	2985 MeV	2990 MeV	2994 MeV
-.4750	19.22±11.52	34.42± 5.08	16.45± 4.12	19.45± 4.93	17.99±3.15	18.71± 4.41	17.17± 2.59	15.22±3.42
-.4250	34.81±10.68	29.29± 4.63	21.76± 3.84	30.09± 4.55	24.37±2.94	21.14± 3.91	15.24± 2.32	17.30±3.07
-.3750	44.36± 9.27	18.69± 3.90	16.68± 3.30	12.63± 3.73	12.59±2.43	17.57± 3.40	18.24± 2.06	16.18±2.67
-.3250	21.77± 7.06	10.47± 2.97	15.86± 2.71	11.54± 2.97	15.86±1.97	5.63± 2.45	16.07± 1.69	12.99±2.09
-.2750	18.83± 5.38	11.73± 2.29	10.53± 2.00	9.73± 2.25	9.34±1.45	6.64± 1.89	8.87± 1.23	6.13±1.46
-.2250	13.69± 3.98	10.89± 1.71	5.62± 1.29	4.05± 1.38	5.37±0.94	4.01± 1.23	5.79± 0.82	5.61±1.04
-.1750	6.03± 2.81	6.69± 1.24	4.27± 0.93	3.45± 1.00	4.25±0.68	3.29± 0.87	3.30± 0.55	3.70±0.73
-.1250	2.06± 2.37	4.71± 1.18	2.88± 0.92	2.17± 0.99	1.64±0.59	3.19± 0.95	1.48± 0.51	2.38±0.70
-.0750	1.85± 2.69	3.11± 1.31	0.14± 1.00	0.70± 1.14	2.05±0.83	1.96± 1.11	2.52± 0.71	0.55±0.80
-.0250	9.61± 3.76	3.07± 1.45	3.41± 1.27	3.85± 1.49	3.34±0.93	4.45± 1.36	2.40± 0.76	3.02±1.03
0.0250	11.00± 3.79	6.07± 1.61	1.21± 1.18	3.96± 1.53	1.90±0.90	2.84± 1.29	1.93± 0.76	1.77±0.97
0.0750	5.23± 2.95	1.88± 1.17	2.54± 1.08	4.50± 1.34	2.22±0.77	3.33± 1.13	2.71± 0.68	1.78±0.83
0.1250	7.06± 2.82	3.52± 1.06	5.41± 1.07	0.41± 0.77	4.04±0.72	4.42± 1.02	3.92± 0.63	2.42±0.69
0.1750	4.98± 2.49	3.15± 0.96	4.29± 0.92	4.04± 1.02	5.00±0.72	3.59± 0.89	3.44± 0.55	2.50±0.62
0.2250	11.58± 3.51	7.59± 1.48	4.23± 1.14	3.18± 1.25	6.45±0.95	2.12± 1.01	4.93± 0.76	4.16±0.89
0.2750	10.60± 4.49	4.29± 1.80	7.23± 1.69	8.68± 2.02	7.67±1.25	8.64± 1.78	8.04± 1.09	9.20±1.43
0.3250	12.01± 5.54	19.81± 2.79	12.50± 2.29	10.27± 2.49	14.03±1.69	6.47± 2.12	8.67± 1.33	10.38±1.78
0.3750	14.49± 7.38	20.54± 3.36	13.49± 2.71	13.15± 3.09	10.91±1.96	16.69± 2.89	15.58± 1.75	11.68±2.20
0.4250	35.52± 9.34	24.85± 3.99	20.33± 3.32	21.75± 3.73	17.61±2.40	20.48± 3.30	18.34± 2.01	18.14±2.59
0.4750	26.57±13.84	26.39± 5.33	21.88± 4.34	27.76± 5.17	25.93±3.25	20.20± 4.30	18.77± 2.59	27.46±3.42

angular distributions which are then converted into differential cross sections.

2. $\pi^0\gamma$

To determine the $\pi^0\gamma$ cross section, the feed-down background is subtracted from data. The primary contribution is from $\pi^0\pi^0$ events in which one of the π^0's decays highly asymmetrically such that the lower energy γ is either below the energy threshold of the central calorimeter or out of the detector geometrical acceptance.

To estimate this background, we simulate $\pi^0\pi^0$ events uniformly distributed in $\cos\theta^*$ and apply the selection algo-

TABLE VII. $\pi^0\gamma$ differential cross section $d\sigma/d\cos\theta^*$(nb) for 3005 MeV$\leq\sqrt{s}\leq$3613 MeV.

$\cos\theta^*_\pi$	3005 MeV	3050 MeV	3097 MeV	3527 MeV	3556 MeV	3591 MeV	3595 MeV	3613 MeV
-.6250				3.17±0.87	3.21±0.68	1.18±0.74	2.00±0.78	2.39±0.65
-.5750				3.68±0.64	3.34±0.47	0.98±0.52	1.75±0.55	2.40±0.47
-.5250			12.07±2.2	1.98±0.48	2.16±0.35	1.56±0.41	0.61±0.39	1.39±0.35
-.4750	7.33±4.15	19.94±6.26	10.31± 1.69	1.83±0.40	1.44±0.27	0.22±0.31	0.97±0.35	1.05±0.30
-.4250	6.36±3.73	5.55±4.87	6.49± 1.37	0.80±0.31	0.56±0.21	0.47±0.28	0.50±0.29	0.44±0.24
-.3750	6.27±3.13	9.48±4.79	6.88± 1.20	0.29±0.24	0.20±0.17	0.42±0.24	0.22±0.25	0.84±0.25
-.3250	1.37±2.38	2.49±3.35	5.82± 0.97	0.53±0.25	0.39±0.17	0.28±0.23	0.50±0.26	0.49±0.22
-.2750	3.75±1.83	9.48±3.20	2.54± 0.71	0.16±0.21	0.39±0.17	0.77±0.27	0.15±0.24	0.67±0.24
-.2250	4.39±1.30	3.23±1.86	3.13± 0.52	0.16±0.21	0.54±0.18	0.00±0.20	0.30±0.25	0.09±0.20
-.1750	2.84±0.86	1.44±0.97	1.92± 0.35	0.60±0.25	0.25±0.18	0.08±0.23	0.27±0.26	0.20±0.21
-.1250	2.33±0.88	1.39±1.16	1.90± 0.37	0.35±0.23	0.46±0.18	0.35±0.24	0.00±0.20	0.12±0.20
-.0750	2.17±1.14	0.57±1.49	1.56± 0.43	0.56±0.25	0.05±0.16	0.27±0.23	0.37±0.24	0.22±0.20
-.0250	-0.14±1.10	2.06±1.84	1.93± 0.50	0.36±0.23	0.58±0.18	0.00±0.18	0.19±0.23	0.39±0.20
0.0250	2.05±1.29	5.07±2.29	1.61± 0.47	0.66±0.25	0.32±0.16	0.04±0.19	0.51±0.25	0.45±0.20
0.0750	1.54±1.04	3.53±1.91	2.00± 0.45	0.39±0.22	0.63±0.18	0.52±0.24	0.03±0.19	0.50±0.21
0.1250	2.82±0.92	0.95±1.02	0.73± 0.27	0.41±0.22	0.44±0.17	0.49±0.24	0.00±0.18	0.40±0.20
0.1750	2.66±0.82	0.39±0.58	1.66± 0.33	0.53±0.23	0.37±0.16	0.10±0.20	0.41±0.24	0.27±0.20
0.2250	4.24±1.21	2.03±1.54	2.95± 0.50	1.27±0.28	0.41±0.15	0.55±0.24	0.18±0.20	0.53±0.20
0.2750	3.88±1.64	4.27±2.39	2.78± 0.64	0.26±0.19	0.63±0.16	0.64±0.23	0.08±0.19	1.00±0.24
0.3250	9.15±2.28	9.30±3.39	6.13± 0.85	0.59±0.22	0.47±0.15	0.54±0.22	0.67±0.24	0.71±0.21
0.3750	7.68±2.57	5.89±3.75	6.36± 1.01	0.90±0.24	0.46±0.16	0.87±0.24	0.58±0.24	0.77±0.21
0.4250	11.53±3.14	14.79±4.57	9.32± 1.17	1.11±0.28	1.13±0.20	0.42±0.22	0.53±0.23	0.89±0.23
0.4750	22.07±4.28	18.17±5.81	10.49± 1.40	1.64±0.34	1.89±0.26	1.11±0.30	1.07±0.30	0.70±0.23
0.5250			11.05±2.27	2.05±0.40	1.63±0.27	1.71±0.35	0.95±0.33	1.63±0.31
0.5750			22.94±18.79	2.72±0.52	2.64±0.37	1.82±0.44	1.86±0.45	1.38±0.36
0.6250				6.53±1.02	3.82±0.65	2.47±0.72	3.21±0.75	2.31±0.59

TABLE VIII. $\pi^0\gamma$ differential cross section $d\sigma/d\cos\theta^*$(nb) for 3616 MeV$\leq\sqrt{s}\leq$3686 MeV.

$\cos\theta^*_\pi$	3616 MeV	3619 MeV	3621 MeV	3686 MeV
-.6250	2.76± 0.62	0.62± 0.86	0.00± 0.55	1.88± 0.80
-.5750	1.85± 0.44	1.01± 0.64	0.00± 0.37	1.92± 0.59
-.5250	1.92± 0.35	1.83± 0.54	0.99± 0.32	1.22± 0.44
-.4750	1.59± 0.30	0.88± 0.42	0.82± 0.28	1.01± 0.38
-.4250	0.47± 0.22	0.05± 0.31	0.00± 0.18	0.42± 0.31
-.3750	0.44± 0.20	0.55± 0.35	0.20± 0.20	0.37± 0.30
-.3250	0.70± 0.22	0.62± 0.34	0.19± 0.20	0.23± 0.29
-.2750	0.00± 0.18	0.58± 0.33	0.22± 0.20	0.68± 0.34
-.2250	0.43± 0.22	0.00± 0.25	0.31± 0.21	0.02± 0.27
-.1750	0.59± 0.22	0.33± 0.32	0.20± 0.19	0.12± 0.28
-.1250	0.34± 0.19	0.59± 0.33	0.00± 0.17	0.15± 0.26
-.0750	0.45± 0.20	0.00± 0.24	0.07± 0.18	0.42± 0.28
-.0250	0.51± 0.20	0.29± 0.28	0.10± 0.17	0.19± 0.24
0.0250	0.20± 0.17	0.05± 0.24	0.00± 0.15	0.00± 0.19
0.0750	0.50± 0.20	0.32± 0.28	0.09± 0.17	0.02± 0.22
0.1250	0.54± 0.19	0.64± 0.31	0.22± 0.17	0.27± 0.25
0.1750	0.78± 0.22	0.00± 0.19	0.14± 0.17	0.47± 0.30
0.2250	0.26± 0.18	0.81± 0.32	0.62± 0.21	0.33± 0.27
0.2750	0.58± 0.20	0.12± 0.24	0.03± 0.16	0.69± 0.31
0.3250	0.74± 0.20	0.58± 0.29	0.42± 0.18	0.47± 0.27
0.3750	0.62± 0.19	0.00± 0.20	0.63± 0.20	0.44± 0.27
0.4250	0.92± 0.22	0.77± 0.32	0.28± 0.18	0.85± 0.31
0.4750	1.20± 0.24	1.16± 0.38	0.57± 0.21	0.53± 0.28
0.5250	1.18± 0.28	1.67± 0.45	1.02± 0.27	1.53± 0.41
0.5750	2.45± 0.38	1.80± 0.56	1.12± 0.34	1.22± 0.46
0.6250	2.66± 0.57	2.51± 0.84	1.29± 0.51	2.04± 0.72

TABLE IX. $\gamma\gamma$ candidates differential cross section $d\sigma/d\cos\theta^*$(nb).

$\cos\theta^*$	2911 MeV	2950 MeV	2975 MeV	2979 MeV	2981 MeV	2985 MeV	2990 MeV	2994 MeV	3005 MeV	3050 MeV
0.0250	$0.00^{+1.11}_{-0.00}$	$0.16^{+0.36}_{-0.13}$	$0.40^{+0.27}_{-0.17}$	$0.40^{+0.53}_{-0.26}$	$0.42^{+0.29}_{-0.18}$	$0.50^{+0.50}_{-0.28}$	$0.86^{+0.24}_{-0.24}$	$0.45^{+0.35}_{-0.21}$	$0.20^{+0.20}_{-0.11}$	$0.30^{+0.69}_{-0.25}$
0.0750	$0.60^{+1.38}_{-0.50}$	$0.47^{+0.46}_{-0.26}$	$0.08^{+0.18}_{-0.07}$	$1.01^{+0.68}_{-0.43}$	$0.85^{+0.36}_{-0.26}$	$0.17^{+0.39}_{-0.14}$	$0.66^{+0.28}_{-0.24}$	$0.56^{+0.37}_{-0.24}$	$0.40^{+0.24}_{-0.16}$	$0.00^{+0.55}_{-0.00}$
0.1250	$0.00^{+1.11}_{-0.00}$	$0.47^{+0.46}_{-0.26}$	$0.48^{+0.29}_{-0.19}$	$0.20^{+0.46}_{-0.17}$	$0.42^{+0.29}_{-0.18}$	$0.50^{+0.50}_{-0.28}$	$0.60^{+0.27}_{-0.19}$	$0.78^{+0.41}_{-0.28}$	$0.33^{+0.23}_{-0.15}$	$0.00^{+0.55}_{-0.00}$
0.1750	$0.60^{+1.38}_{-0.50}$	$0.79^{+0.53}_{-0.34}$	$0.48^{+0.29}_{-0.19}$	$0.20^{+0.46}_{-0.17}$	$0.93^{+0.38}_{-0.28}$	$0.50^{+0.50}_{-0.28}$	$0.73^{+0.29}_{-0.22}$	$0.56^{+0.37}_{-0.24}$	$0.33^{+0.23}_{-0.15}$	$0.30^{+0.69}_{-0.25}$
0.2250	$0.00^{+1.11}_{-0.00}$	$0.79^{+0.53}_{-0.34}$	$0.72^{+0.33}_{-0.24}$	$0.40^{+0.53}_{-0.26}$	$0.76^{+0.35}_{-0.25}$	$0.34^{+0.45}_{-0.22}$	$0.33^{+0.22}_{-0.14}$	$0.67^{+0.39}_{-0.26}$	$0.46^{+0.26}_{-0.17}$	$0.00^{+0.55}_{-0.00}$
0.2750	$0.60^{+1.38}_{-0.50}$	$1.42^{+0.65}_{-0.46}$	$1.28^{+0.32}_{-0.32}$	$1.01^{+0.68}_{-0.43}$	$0.76^{+0.35}_{-0.25}$	$1.34^{+0.67}_{-0.47}$	$0.79^{+0.30}_{-0.22}$	$0.56^{+0.37}_{-0.24}$	$0.93^{+0.25}_{-0.25}$	$0.30^{+0.69}_{-0.25}$
0.3250	$4.76^{+2.37}_{-1.66}$	$2.05^{+0.57}_{-0.57}$	$1.44^{+0.34}_{-0.34}$	$1.61^{+0.79}_{-0.55}$	$2.11^{+0.42}_{-0.42}$	$2.01^{+0.78}_{-0.58}$	$1.46^{+0.31}_{-0.31}$	$2.11^{+0.49}_{-0.49}$	$1.86^{+0.35}_{-0.35}$	$0.89^{+0.88}_{-0.49}$
0.3750	$1.79^{+1.75}_{-0.98}$	$3.16^{+0.71}_{-0.71}$	$2.48^{+0.45}_{-0.45}$	$2.82^{+0.75}_{-0.75}$	$2.28^{+0.44}_{-0.44}$	$1.84^{+0.75}_{-0.56}$	$2.38^{+0.40}_{-0.40}$	$2.00^{+0.47}_{-0.47}$	$2.06^{+0.37}_{-0.37}$	$0.89^{+0.88}_{-0.49}$

$\cos\theta^*$	3097 MeV	3527 MeV	3556 MeV	3591 MeV	3595 MeV	3613 MeV	3616 MeV	3619 MeV	3621 MeV	3686 MeV
0.0250	$0.17^{+0.17}_{-0.10}$	$0.05^{+0.01}_{-0.01}$	$0.04^{+0.04}_{-0.02}$	$0.00^{+0.07}_{-0.00}$	$0.00^{+0.09}_{-0.00}$	$0.03^{+0.07}_{-0.02}$	$0.00^{+0.05}_{-0.00}$	$0.00^{+0.13}_{-0.00}$	$0.00^{+0.05}_{-0.00}$	$0.04^{+0.09}_{-0.03}$
0.0750	$0.12^{+0.16}_{-0.08}$	$0.04^{+0.01}_{-0.01}$	$0.03^{+0.03}_{-0.02}$	$0.00^{+0.07}_{-0.00}$	$0.09^{+0.13}_{-0.06}$	$0.03^{+0.07}_{-0.02}$	$0.06^{+0.08}_{-0.04}$	$0.07^{+0.16}_{-0.06}$	$0.00^{+0.05}_{-0.00}$	$0.04^{+0.09}_{-0.03}$
0.1250	$0.06^{+0.14}_{-0.05}$	$0.03^{+0.01}_{-0.01}$	$0.07^{+0.04}_{-0.03}$	$0.12^{+0.12}_{-0.07}$	$0.05^{+0.12}_{-0.04}$	$0.00^{+0.05}_{-0.00}$	$0.03^{+0.07}_{-0.03}$	$0.00^{+0.13}_{-0.00}$	$0.06^{+0.08}_{-0.04}$	$0.00^{+0.07}_{-0.00}$
0.1750	$0.12^{+0.16}_{-0.08}$	$0.05^{+0.01}_{-0.01}$	$0.18^{+0.05}_{-0.05}$	$0.00^{+0.07}_{-0.00}$	$0.09^{+0.13}_{-0.06}$	$0.00^{+0.05}_{-0.00}$	$0.00^{+0.05}_{-0.00}$	$0.14^{+0.18}_{-0.09}$	$0.03^{+0.07}_{-0.02}$	$0.00^{+0.09}_{-0.03}$
0.2250	$0.17^{+0.17}_{-0.10}$	$0.04^{+0.01}_{-0.01}$	$0.12^{+0.05}_{-0.04}$	$0.00^{+0.07}_{-0.00}$	$0.00^{+0.09}_{-0.00}$	$0.00^{+0.05}_{-0.00}$	$0.09^{+0.09}_{-0.05}$	$0.00^{+0.13}_{-0.00}$	$0.03^{+0.07}_{-0.02}$	$0.04^{+0.09}_{-0.03}$
0.2750	$0.64^{+0.26}_{-0.20}$	$0.05^{+0.01}_{-0.01}$	$0.07^{+0.04}_{-0.03}$	$0.00^{+0.07}_{-0.00}$	$0.00^{+0.09}_{-0.00}$	$0.00^{+0.05}_{-0.00}$	$0.03^{+0.07}_{-0.03}$	$0.00^{+0.13}_{-0.00}$	$0.06^{+0.08}_{-0.04}$	$0.04^{+0.09}_{-0.03}$
0.3250	$0.70^{+0.27}_{-0.20}$	$0.05^{+0.01}_{-0.01}$	$0.06^{+0.04}_{-0.02}$	$0.04^{+0.09}_{-0.03}$	$0.05^{+0.12}_{-0.04}$	$0.00^{+0.05}_{-0.00}$	$0.06^{+0.08}_{-0.04}$	$0.00^{+0.13}_{-0.00}$	$0.03^{+0.07}_{-0.02}$	$0.04^{+0.11}_{-0.05}$
0.3750	$0.64^{+0.26}_{-0.20}$	$0.06^{+0.01}_{-0.01}$	$0.10^{+0.05}_{-0.04}$	$0.00^{+0.07}_{-0.00}$	$0.05^{+0.12}_{-0.04}$	$0.00^{+0.05}_{-0.00}$	$0.00^{+0.05}_{-0.00}$	$0.07^{+0.16}_{-0.06}$	$0.16^{+0.10}_{-0.06}$	$0.08^{+0.07}_{-0.00}$
0.4250	$1.22^{+0.27}_{-0.27}$	$0.09^{+0.01}_{-0.01}$	$0.12^{+0.05}_{-0.04}$	$0.04^{+0.09}_{-0.03}$	$0.05^{+0.12}_{-0.04}$	$0.00^{+0.05}_{-0.00}$	$0.03^{+0.07}_{-0.03}$	$0.00^{+0.13}_{-0.00}$	$0.06^{+0.08}_{-0.04}$	$0.00^{+0.09}_{-0.03}$
0.4750	$1.97^{+0.34}_{-0.34}$	$0.21^{+0.02}_{-0.02}$	$0.16^{+0.06}_{-0.04}$	$0.04^{+0.09}_{-0.03}$	$0.05^{+0.12}_{-0.04}$	$0.00^{+0.05}_{-0.00}$	$0.03^{+0.07}_{-0.03}$	$0.00^{+0.13}_{-0.00}$	$0.06^{+0.08}_{-0.04}$	$0.04^{+0.11}_{-0.05}$
0.5250		$0.22^{+0.02}_{-0.02}$	$0.21^{+0.06}_{-0.06}$	$0.16^{+0.13}_{-0.08}$	$0.27^{+0.17}_{-0.11}$	$0.13^{+0.09}_{-0.06}$	$0.06^{+0.08}_{-0.04}$	$0.21^{+0.20}_{-0.11}$	$0.22^{+0.11}_{-0.08}$	$0.08^{+0.11}_{-0.05}$
0.5750		$0.45^{+0.03}_{-0.03}$	$0.43^{+0.08}_{-0.06}$	$0.29^{+0.15}_{-0.10}$	$0.32^{+0.18}_{-0.12}$	$0.16^{+0.10}_{-0.06}$	$0.37^{+0.14}_{-0.10}$	$0.21^{+0.20}_{-0.11}$	$0.22^{+0.11}_{-0.08}$	$0.08^{+0.16}_{-0.05}$
0.6250		$0.87^{+0.05}_{-0.05}$	$0.86^{+0.11}_{-0.11}$	$0.78^{+0.18}_{-0.18}$	$0.32^{+0.18}_{-0.12}$	$0.48^{+0.12}_{-0.12}$	$0.55^{+0.13}_{-0.13}$	$0.34^{+0.24}_{-0.15}$	$0.44^{+0.12}_{-0.12}$	$0.69^{+0.18}_{-0.18}$

TABLE X. Feed-down to $\gamma\gamma$ differential cross section $d\sigma/d\cos\theta^*$(nb) from $\pi^0\pi^0$ and $\pi^0\gamma$.

$\cos\theta^*$	2911 MeV	2950 MeV	2975 MeV	2979 MeV	2981 MeV	2985 MeV	2990 MeV	2994 MeV	3005 MeV	3050 MeV
0.0250	0.83 ± 0.16	0.45 ± 0.06	0.26 ± 0.05	0.35 ± 0.06	0.28 ± 0.04	0.33 ± 0.05	0.24 ± 0.03	0.25 ± 0.04	0.16 ± 0.05	0.27 ± 0.09
0.0750	0.37 ± 0.12	0.28 ± 0.05	0.17 ± 0.04	0.24 ± 0.05	0.22 ± 0.03	0.24 ± 0.05	0.23 ± 0.03	0.15 ± 0.03	0.18 ± 0.05	0.16 ± 0.07
0.1250	0.40 ± 0.12	0.33 ± 0.05	0.30 ± 0.04	0.13 ± 0.04	0.22 ± 0.03	0.27 ± 0.04	0.21 ± 0.02	0.18 ± 0.03	0.19 ± 0.04	0.08 ± 0.05
0.1750	0.49 ± 0.13	0.38 ± 0.05	0.30 ± 0.04	0.27 ± 0.04	0.32 ± 0.03	0.24 ± 0.04	0.24 ± 0.02	0.22 ± 0.03	0.19 ± 0.04	0.06 ± 0.03
0.2250	1.13 ± 0.19	0.78 ± 0.08	0.43 ± 0.06	0.34 ± 0.06	0.49 ± 0.04	0.30 ± 0.05	0.44 ± 0.04	0.40 ± 0.05	0.36 ± 0.06	0.21 ± 0.08
0.2750	1.67 ± 0.27	0.98 ± 0.10	0.92 ± 0.09	0.95 ± 0.11	0.89 ± 0.07	0.81 ± 0.09	0.86 ± 0.06	0.79 ± 0.07	0.51 ± 0.09	0.59 ± 0.13
0.3250	2.53 ± 0.37	1.94 ± 0.16	1.70 ± 0.13	1.44 ± 0.15	1.73 ± 0.10	1.05 ± 0.12	1.47 ± 0.08	1.41 ± 0.10	0.90 ± 0.12	0.71 ± 0.17
0.3750	4.77 ± 0.53	2.96 ± 0.21	2.29 ± 0.17	2.11 ± 0.20	2.00 ± 0.13	2.39 ± 0.18	2.31 ± 0.11	2.04 ± 0.14	1.41 ± 0.16	1.09 ± 0.24
0.4250	6.47 ± 0.67	4.18 ± 0.27	3.31 ± 0.22	3.65 ± 0.26	3.27 ± 0.17	3.16 ± 0.22	2.73 ± 0.13	2.81 ± 0.17	1.97 ± 0.21	1.46 ± 0.28
0.4750	6.19 ± 0.91	5.13 ± 0.35	3.74 ± 0.28	4.19 ± 0.34	3.96 ± 0.21	3.65 ± 0.29	3.45 ± 0.17	3.71 ± 0.23	2.97 ± 0.28	2.55 ± 0.39
0.5250		4.97 ± 1.36	5.04 ± 0.81	2.81 ± 0.85	4.28 ± 0.56	5.34 ± 0.75	2.06 ± 0.72	4.98 ± 0.53	3.75 ± 0.64	2.98 ± 0.65

$\cos\theta^*$	3097 MeV	3527 MeV	3556 MeV	3591 MeV	3595 MeV	3613 MeV	3616 MeV	3619 MeV	3621 MeV	3686 MeV
0.0250	0.14 ± 0.02	0.04 ± 0.01	0.03 ± 0.01	0.01 ± 0.01	0.03 ± 0.01	0.03 ± 0.01	0.03 ± 0.01	0.02 ± 0.01	0.01 ± 0.01	0.01 ± 0.01
0.0750	0.13 ± 0.02	0.04 ± 0.01	0.03 ± 0.01	0.03 ± 0.01	0.02 ± 0.01	0.03 ± 0.01	0.03 ± 0.01	0.02 ± 0.01	0.01 ± 0.01	0.02 ± 0.01
0.1250	0.09 ± 0.01	0.03 ± 0.01	0.04 ± 0.01	0.03 ± 0.01	0.01 ± 0.01	0.02 ± 0.01	0.03 ± 0.01	0.04 ± 0.01	0.01 ± 0.01	0.02 ± 0.01
0.1750	0.11 ± 0.01	0.04 ± 0.01	0.03 ± 0.01	0.02 ± 0.01	0.03 ± 0.01	0.02 ± 0.01	0.05 ± 0.01	0.02 ± 0.01	0.02 ± 0.01	0.03 ± 0.01
0.2250	0.22 ± 0.02	0.05 ± 0.01	0.04 ± 0.01	0.03 ± 0.01	0.02 ± 0.01	0.03 ± 0.01	0.03 ± 0.01	0.03 ± 0.01	0.03 ± 0.01	0.03 ± 0.01
0.2750	0.29 ± 0.03	0.02 ± 0.01	0.04 ± 0.01	0.05 ± 0.01	0.02 ± 0.01	0.06 ± 0.01	0.03 ± 0.01	0.03 ± 0.01	0.02 ± 0.01	0.05 ± 0.01
0.3250	0.64 ± 0.05	0.05 ± 0.01	0.04 ± 0.01	0.04 ± 0.01	0.04 ± 0.01	0.05 ± 0.01	0.05 ± 0.01	0.05 ± 0.01	0.03 ± 0.01	0.03 ± 0.01
0.3750	0.85 ± 0.06	0.05 ± 0.01	0.04 ± 0.01	0.05 ± 0.01	0.04 ± 0.01	0.06 ± 0.01	0.04 ± 0.01	0.03 ± 0.01	0.04 ± 0.01	0.04 ± 0.01
0.4250	1.14 ± 0.08	0.09 ± 0.01	0.08 ± 0.01	0.05 ± 0.01	0.05 ± 0.01	0.06 ± 0.01	0.06 ± 0.01	0.04 ± 0.01	0.03 ± 0.01	0.05 ± 0.01
0.4750	1.62 ± 0.10	0.18 ± 0.02	0.15 ± 0.01	0.08 ± 0.01	0.10 ± 0.02	0.09 ± 0.01	0.12 ± 0.01	0.10 ± 0.02	0.08 ± 0.01	0.07 ± 0.02
0.5250	2.36 ± 0.16	0.26 ± 0.03	0.21 ± 0.02	0.18 ± 0.02	0.12 ± 0.02	0.17 ± 0.02	0.18 ± 0.02	0.19 ± 0.03	0.13 ± 0.02	0.14 ± 0.02
0.5750		0.52 ± 0.04	0.41 ± 0.03	0.24 ± 0.03	0.31 ± 0.03	0.31 ± 0.03	0.31 ± 0.03	0.27 ± 0.04	0.16 ± 0.02	0.25 ± 0.03
0.6250		1.14 ± 0.07	0.71 ± 0.05	0.45 ± 0.06	0.70 ± 0.06	0.67 ± 0.05	0.59 ± 0.05	0.54 ± 0.07	0.32 ± 0.04	0.57 ± 0.06
0.6750		2.66 ± 0.47	2.48 ± 0.28	1.92 ± 0.24	2.74 ± 0.24	2.36 ± 0.19	1.99 ± 0.15	2.06 ± 0.23	1.05 ± 0.14	2.19 ± 0.16

rithm for $\pi^0\gamma$. The probability for $\pi^0\pi^0$ to be selected as $\pi^0\gamma$ is given in Fig. 7(b) for $\sqrt{s}=2.990$ GeV as a function of θ^*_γ, where θ^*_γ refers to the c.m. angle of the γ. Because of the Lorentz boost, the forward going π^0 has the greater energy and the opening angle for the $\gamma\gamma$ pair is smaller than for the backward going π^0. The backward π^0 is more likely to lose a γ out the back of the detector or below threshold and be reconstructed as a single γ, as seen in Fig. 7(b). To obtain the background to $\pi^0\gamma$ [dotted line in Fig. 7(c)], the measured $\pi^0\pi^0$ cross section, plotted for $\cos\theta^*$ between -0.5 to 0.5 as if the π^0's were not identical, Fig. 7(a), is multiplied by the probability for misidentification as $\pi^0\gamma$. This background is subtracted from the $\pi^0\gamma$ candidates in angular intervals of size $\Delta\cos\theta^*=0.025$ to give the $\pi^0\gamma$ signal with statistical errors shown in Fig. 7(d). The data are corrected with the combined efficiency for $\pi^0\gamma$, given in Fig. 7(e), and divided by integrated luminosity to obtain the differential cross section, Fig. 7(f).

The $\pi^0\gamma$ cross-section determination is sensitive to the Monte Carlo determination of the misidentification probability. We observe that, while the $\pi^0\gamma$ candidate angular distribution is strongly peaked backward, the $\pi^0\gamma$ differential

TABLE XI. $\pi^0\eta$ differential cross section $d\sigma/d\cos\theta^*$(nb) for 2911 MeV$\leq\sqrt{s}\leq$2990 MeV.

$\cos\theta^*_\pi$	2911 MeV
-.450	888.33±53.47
-.350	364.91±23.03
-.250	262.13±18.77
-.150	323.37±21.61
-.050	330.18±21.96
0.050	300.48±21.52
0.150	254.71±20.26
0.250	199.68±17.86
0.350	246.02±22.84
0.450	750.50±63.89

$\cos\theta^*_\pi$	2950 MeV	2975 MeV	2979 MeV	2981 MeV	2985 MeV	2990 MeV
-.475	730.04±31.74	541.67±16.93	571.02±27.41	511.62±15.91	522.18±22.64	539.90±16.28
-.425	388.63±16.77	307.20± 9.91	334.72±16.91	284.20± 9.44	245.24±12.32	299.40± 9.69
-.375	223.97±11.49	148.31± 6.21	186.55±11.19	156.38± 6.38	152.42± 8.79	158.67± 6.61
-.325	168.10± 9.55	110.40± 5.19	107.46± 8.44	100.94± 5.02	99.48± 6.86	108.62± 5.27
-.275	178.03± 9.73	125.03± 5.61	132.57± 9.40	130.98± 5.70	117.69± 7.76	114.23± 5.37
-.225	201.10±10.47	163.07± 6.48	132.98± 9.27	159.60± 6.37	142.51± 8.27	153.74± 6.31
-.175	244.69±11.41	196.40± 7.22	176.72±10.68	186.47± 6.94	185.20± 9.77	178.28± 6.67
-.125	260.33±12.12	216.11± 7.67	229.61±12.82	229.26± 7.85	205.56±10.53	204.16± 7.39
-.075	274.07±12.52	224.68± 7.75	202.52±11.73	225.75± 7.84	207.08±10.39	200.25± 7.35
-.025	290.65±13.14	225.83± 7.95	241.82±13.17	228.91± 7.91	233.18±11.31	219.12± 7.80
0.025	263.27±12.34	227.88± 7.92	232.19±12.86	238.78± 8.09	226.21±10.90	223.73± 7.94
0.075	251.74±12.31	238.33± 8.42	247.84±13.64	242.72± 8.41	214.13±11.09	223.68± 8.02
0.125	260.76±12.82	223.65± 8.12	208.10±12.35	199.49± 7.43	186.98±10.25	197.73± 7.55
0.175	233.82±12.14	195.19± 7.64	192.75±12.07	180.31± 7.25	182.93±10.56	183.72± 7.46
0.225	220.66±12.11	168.40± 7.37	130.37± 9.83	154.57± 6.77	150.36± 9.53	144.71± 6.72
0.275	157.05±10.45	107.12± 5.69	122.81± 9.80	114.50± 6.04	114.52± 8.24	107.09± 5.89
0.325	150.24±10.81	100.47± 5.65	129.00±10.50	107.88± 5.99	106.52± 8.56	102.82± 6.01
0.375	214.19±14.41	173.87± 8.68	147.55±12.21	146.95± 7.60	152.05±11.09	152.65± 8.17
0.425	376.64±22.75	266.88±12.08	345.02±22.90	263.46±12.18	247.17±16.06	282.95±12.97
0.475	646.67±38.04	463.97±20.13	565.58±36.28	559.55±23.40	548.61±31.83	520.04±22.00

TABLE XII. $\pi^0\eta$ differential cross section $d\sigma/d\cos\theta^*$(nb) for 2994 MeV$\leqslant\sqrt{s}\leqslant$4274 MeV.

$\cos\theta^*_\pi$	2994 MeV	3005 MeV	3097 MeV	3526 MeV
-.525	716.65±53.57	534.22±51.17	389.29± 14.17	28.31± 0.82
-.475	432.96±16.55	395.36±20.87	231.15± 7.63	10.13± 0.46
-.425	264.06±10.71	253.56±14.07	109.47± 4.72	12.49± 0.52
-.375	138.28± 7.26	114.40± 8.60	51.52± 3.03	14.31± 0.55
-.325	79.99± 5.29	84.04± 7.34	38.38± 2.65	14.07± 0.54
-.275	93.39± 5.60	88.56± 7.28	51.90± 3.05	12.29± 0.50
-.225	128.24± 6.67	107.60± 7.87	73.64± 3.61	10.61± 0.48
-.175	170.49± 7.71	161.27±10.06	88.08± 4.10	6.73± 0.38
-.125	198.51± 8.62	155.87±10.00	82.78± 3.95	4.41± 0.30
-.075	205.47± 8.88	158.82±10.27	88.51± 4.18	3.45± 0.26
-.025	198.16± 8.67	182.44±11.00	94.98± 4.30	2.64± 0.23
0.025	187.67± 8.38	188.63±11.70	94.39± 4.36	2.61± 0.22
0.075	195.16± 8.65	196.65±11.88	86.45± 4.10	3.57± 0.27
0.125	184.32± 8.58	161.45±10.49	97.22± 4.47	5.52± 0.33
0.175	161.35± 8.06	168.55±11.26	91.33± 4.32	7.03± 0.38
0.225	126.68± 7.17	117.31± 9.25	76.82± 4.11	9.63± 0.45
0.275	88.23± 6.00	103.98± 9.23	54.50± 3.41	12.63± 0.53
0.325	79.24± 5.83	64.54± 6.92	39.77± 3.00	14.01± 0.55
0.375	127.18± 8.54	113.17±10.37	48.00± 3.50	13.67± 0.57
0.425	224.68±12.82	218.68±16.67	108.53± 5.92	11.45± 0.52
0.475	425.16±22.07	409.81±28.48	222.83± 10.15	12.81± 0.58
0.525	802.27±47.77	696.90±53.93	410.95± 17.44	27.97± 0.92
0.575			703.08± 43.19	86.77± 1.97
0.625				200.01± 3.91
0.675				402.65±11.82

$\cos\theta^*_\pi$	3592 MeV
-.650	98.66±4.30
-.550	18.68±0.91
-.450	4.80±0.41
-.350	5.29±0.42
-.250	4.65±0.40
-.150	1.53±0.22
-.050	1.72±0.23
0.050	1.82±0.24
0.150	2.23±0.27
0.250	3.94±0.37
0.350	5.85±0.46
0.450	5.85±0.51
0.550	19.22±1.03
0.650	110.20±4.49

$\cos\theta^*_\pi$	3617 MeV
-.625	60.60±2.01
-.575	23.82±1.01
-.525	7.12±0.49
-.475	4.42±0.36
-.425	4.97±0.41
-.375	5.82±0.42
-.325	5.69±0.43
-.275	4.24±0.37
-.225	3.44±0.34
-.175	2.42±0.26
-.125	1.83±0.22
-.075	1.76±0.24
-.025	1.55±0.22
0.025	1.54±0.21
0.075	1.50±0.20
0.125	1.57±0.22
0.175	2.05±0.24
0.225	3.22±0.33
0.275	3.72±0.34
0.325	5.40±0.42
0.375	5.29±0.42
0.425	5.10±0.42
0.475	4.88±0.42
0.525	8.34±0.59
0.575	23.80±1.12
0.625	59.19±2.23

$\cos\theta^*_\pi$	4274 MeV
-.550	$1.16^{+0.78}_{-0.50}$
-.450	$0.99^{+0.67}_{-0.43}$
-.350	$0.39^{+0.51}_{-0.25}$
-.250	$0.39^{+0.51}_{-0.25}$
-.150	$0.00^{+0.36}_{-0.00}$
-.050	$0.20^{+0.47}_{-0.17}$
0.050	$0.40^{+0.53}_{-0.26}$
0.150	$0.00^{+0.36}_{-0.00}$
0.250	$0.19^{+0.45}_{-0.16}$
0.350	$0.17^{+0.40}_{-0.14}$
0.450	$1.00^{+0.60}_{-0.40}$
0.550	$0.90^{+0.61}_{-0.39}$
0.650	$0.39^{+0.89}_{-0.32}$

TABLE XIII. $\eta\eta$ differential cross section $d\sigma/d\cos\theta^*$(nb).

$\cos\theta^*$	2911 MeV
0.050	287.44± 36.21
0.150	428.42± 44.67
0.250	439.82± 48.28
0.350	589.90± 66.37
0.450	1203.85±136.31

$\cos\theta^*$	2950 MeV	2975 MeV	2979 MeV	2981 MeV	2985 MeV	2990 MeV
0.025	193.12± 18.01	158.74±11.31	182.41± 19.44	147.10±10.93	167.80± 16.78	124.97± 9.50
0.075	230.23± 19.96	176.09±12.04	193.42± 20.28	163.81±11.55	161.01± 16.61	151.64±10.75
0.125	246.47± 20.76	196.39±12.92	177.14± 19.21	180.71±12.21	170.08± 17.01	155.45±10.65
0.175	282.37± 22.54	220.93±13.95	170.62± 19.08	160.57±11.56	187.62± 17.81	153.74±10.84
0.225	283.60± 23.31	219.63±14.33	229.78± 23.21	171.87±12.15	169.69± 17.32	154.19±11.31
0.275	290.78± 24.66	218.71±14.85	202.50± 22.36	188.12±13.37	154.57± 16.77	162.88±11.88
0.325	376.97± 30.18	283.18±17.95	248.42± 26.19	237.59±16.09	231.27± 22.05	220.53±15.18
0.375	485.65± 37.25	345.39±21.80	391.53± 36.20	368.88±21.97	391.62± 32.63	335.00±20.39
0.425	600.43± 47.62	618.08±32.99	525.96± 48.01	640.66±33.17	600.45± 45.65	558.20±30.54
0.475	905.62± 76.00	818.67±47.34	872.67± 76.54	876.45±47.60	821.20± 64.32	854.50±45.42
0.525	1393.89±157.83	936.16±76.44	1200.29±135.91	1126.67±83.06	1163.81±117.56	1016.55±72.80

$\cos\theta^*$	2994 MeV	3005 MeV	3097 MeV	3526 MeV
0.025	140.00±12.47	135.82± 16.23	42.30± 4.64	6.58± 0.57
0.075	139.74±12.50	113.17± 14.99	39.79± 4.59	9.06± 0.68
0.125	149.47±12.91	98.49± 14.07	46.39± 4.94	12.26± 0.79
0.175	159.55±13.53	148.79± 17.78	41.18± 4.63	13.02± 0.82
0.225	133.47±12.73	138.36± 17.43	37.99± 4.54	12.60± 0.81
0.275	128.63±12.99	124.40± 17.25	43.37± 5.08	11.10± 0.76
0.325	210.86±17.76	203.51± 23.19	77.42± 7.25	11.33± 0.80
0.375	289.22±22.38	299.89± 30.77	191.65±12.40	13.19± 0.89
0.425	507.61±34.07	508.31± 46.40	304.63±17.08	20.82± 1.18
0.475	767.85±51.30	808.86± 71.49	484.60±25.33	38.74± 1.75
0.525	961.70±85.34	1176.03±124.66	602.26±36.72	69.45± 2.62
0.575			961.94±84.37	115.25± 4.02
0.625				197.53± 7.15
0.675				328.57±19.20

$\cos\theta^*$	3592 MeV
0.050	4.76±0.63
0.150	5.32±0.67
0.250	5.18±0.67
0.350	4.22±0.64
0.450	10.18±1.09
0.550	31.40±2.44
0.650	116.34±8.82

$\cos\theta^*$	3617 MeV
0.025	4.25±0.57
0.075	3.65±0.52
0.125	3.86±0.53
0.175	4.56±0.59
0.225	4.93±0.63
0.275	4.79±0.63
0.325	4.70±0.64
0.375	4.87±0.68
0.425	6.47±0.81
0.475	11.35±1.13
0.525	20.16±1.67
0.575	37.45±2.66
0.625	76.24±5.03
0.675	88.80±9.31

$\cos\theta^*$	4274 MeV
0.100	$0.34^{+0.45}_{-0.22}$
0.300	$0.18^{+0.42}_{-0.15}$
0.500	$1.03^{+0.81}_{-0.49}$
0.700	$3.68^{+4.86}_{-2.38}$

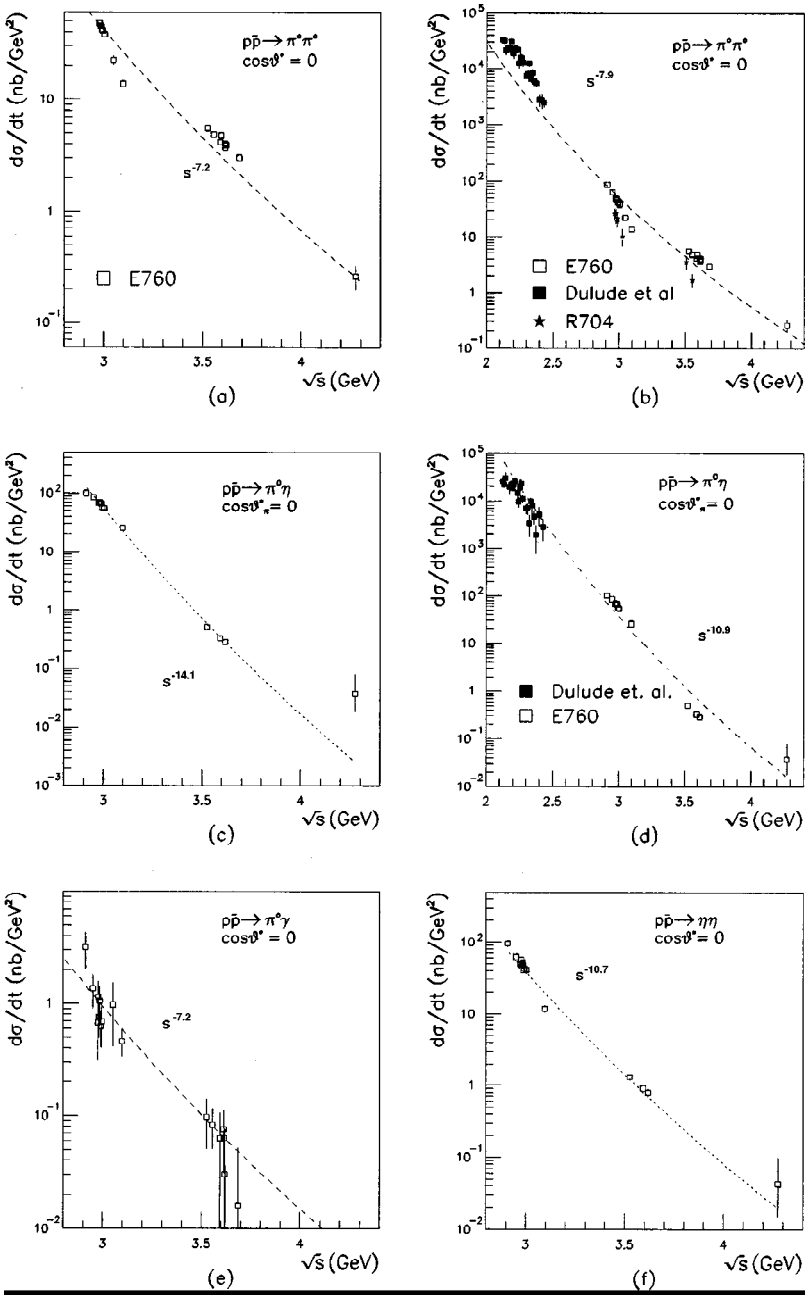

FIG. 16. $d\sigma/dt$ at $\cos\theta^*=0$ for $\pi^0\pi^0$, $\eta\pi^0$, $\pi^0\gamma$, and $\eta\eta$. The curves are fits to a power-law form. Results of [6] and [1] are used in the fit in (b) and those of [6] are used in the fit to (d).

cross section is consistent with forward-backward symmetry as required by charge conjugation invariance. Figure 7(g) gives the ratio of the differential cross section for positive $\cos\theta^*$ to that for negative $\cos\theta^*$, which illustrates this point.

3. $\gamma\gamma$

Backgrounds to the $\gamma\gamma$ channel are discussed in detail in Ref. [17]. A method similar to the $\pi^0\gamma$ analysis is used to calculate the feed-down to $\gamma\gamma$ from $\pi^0\gamma$ and $\pi^0\pi^0$. The probabilities for a $\pi^0\gamma$ or $\pi^0\pi^0$ event to be selected as a $\gamma\gamma$ event are estimated by simulation. The resulting distributions are fit to polynomials, Figs. 7(h) and 7(i). The measured differential cross sections for $\pi^0\gamma$ [Fig. 7(f)] and $\pi^0\pi^0$ [Fig. 7(a)] are multiplied, respectively, by the misidentification probabilities to yield backgrounds to $\gamma\gamma$. The backgrounds from $\pi^0\gamma$ and $\pi^0\pi^0$ feed-down are approximately equal, Figs. 7(j) and 7(k). The cross sections for $\gamma\gamma$ candidates and feed-down background are given in Fig. 7(l) in angular intervals of size $\Delta\cos\theta^*=0.05$. The difference between the candidate and feed-down cross sections is attributed to the $\gamma\gamma$ final state. We see a clear signal at 2.990 and 2.994 GeV due to the $\gamma\gamma$ decay of the η_c [17] and at 3.556 GeV due to the $\gamma\gamma$ decay of the χ_2 [31].

4. $\eta\pi^0$ and $\eta\eta$

We estimate the background to $\eta\pi^0$ from the $\pi^0\pi^0\pi^0$, $\pi^0\pi^0\eta$, $\pi^0\eta\eta$, and $\eta\omega$ channels by simulation in analogy to the $\pi^0\pi^0$ analysis. We use our measured cross sections [29,30] and extrapolate angular distributions where the data is unavailable. The simulated background accounts for approximately one-third of the observed background as shown in Fig. 8. Much of the remaining background is expected to be combinatoric, for which the wrong γ's are paired. Using a method similar to that based on the *akinematic* distributions

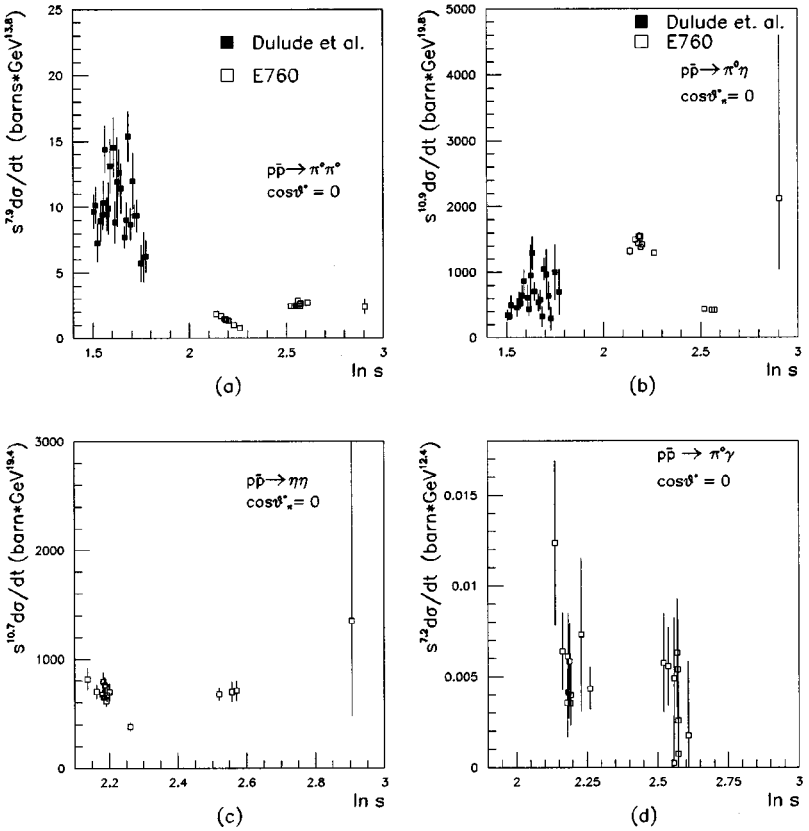

FIG. 17. $s^{n(d\sigma/dt)}$ at $\cos\theta^*=0$ for $\pi^0\pi^0$, $\eta\pi^0$, $\eta\eta$, and $\pi^0\gamma$, where n is obtained from fits to a power-law form.

for the $\pi^0\pi^0$ data, at each $E_{\text{c.m.}}$ for angular intervals of $\Delta\cos\theta^*=0.05$ or $\Delta\cos\theta^*=0.1$, depending upon the number of events, we fit the M_X (unconstrained $\gamma\gamma$ mass) distribution to a Gaussian signal plus constant background and subtract background events. The background level is 4–10 % at all energies.

The background to $\eta\eta$ from $\pi^0\eta\eta$ is studied by simulation and found to be negligible. The background as observed in the M_X distribution is fit and subtracted just as for the $\eta\pi^0$ channel.

J. Systematic uncertainty

The overall systematic uncertainty in the differential cross sections includes estimated uncertainties in the following: luminosity measurement, 4% [21]; trigger efficiencies, due to uncertainty in the energy and rate dependence of random hits in H1, FCH, and FCAL, 1%; filter efficiency, due to uncertainty in identification of out-of-time clusters, 3%; CCAL energy threshold, see below, 1%; accuracy of the Monte Carlo simulation in modeling kinematic distributions, leading to errors in efficiencies and in background estimation, see below, 3%.

We study the effects of changing the *akinematics* and *acoplanarity* cuts and CCAL cluster energy threshold on the $\pi^0\pi^0$ and $\eta\pi^0$ differential cross sections at 2.990 and 3.591 GeV. For $\pi^0\pi^0$ at 2.990 GeV, Fig. 9 shows the effects of separately varying the *akinematics* and *acoplanarity* cuts from 0.01 to 0.025 and 0.02 to 0.04, respectively. The average differential cross section changes by 3% or less. Figure 10 shows the effect of changing the CCAL threshold from 50 to 100 MeV. The average differential cross section changes by less than 1%. Since the components of the systematic uncertainty are uncorrelated, we recombine them in quadrature to obtain a total systematic uncertainty of 6%.

A similar computation for the $\eta\pi^0$ and $\eta\eta$ systematic uncertainties includes larger uncertainties in trigger efficiencies resulting in a 7% total. The systematic uncertainty for $\gamma\gamma$ is increased by the use of a CCAL cluster energy threshold of 20 MeV, to which the feed-down background is sensitive. This threshold has an uncertainty of about 5 MeV. We simulate the effect of a 5 MeV increase and find that $\gamma\gamma$ cross sections decrease by approximately 12% [17].

IV. RESULTS

In Figs. 11–15, we plot the differential cross sections $d\sigma/d\cos\theta^*$ for the channels studied in the center-of-mass energy range $2.911\leqslant\sqrt{s}\leqslant4.274$ GeV. For the $\gamma\gamma$ channel, we give the differential cross sections for the candidate events and for the simulated feed-down background. These results are tabulated in Tables III–XIII. In Fig. 13, in the 2990 and 2994 MeV plots, we clearly observe an excess cross section for $\cos\theta^*\leqslant0.3$ due to the $\gamma\gamma$ decay of the η_c (see Ref. [17] for details), and in the 3556 MeV plot, due to the $\gamma\gamma$ decay of the χ_2 (see Ref. [31] for details). At other energies, the simulated background consistently accounts for the data, and we therefore obtain an upper limit for continuum annihilation to $\gamma\gamma$, discussed in Ref. [17].

The differential cross sections for these reactions have distinctive features. For $\pi^0\pi^0$ annihilations with $2.911\leqslant\sqrt{s}\leqslant3.097$ GeV, $d\sigma/d\cos\theta^*$ falls with increasing θ^* to a minimum at $\cos^*=0.16$, rising to a secondary maximum at $\cos\theta^*=0$. The cross section at small $\cos\theta^*$ decreases rapidly with $\sqrt{s}$, increasing the depth of the minimum. For $3.524\leqslant\sqrt{s}\leqslant3.686$ GeV, $d\sigma/d\cos\theta^*$ is nearly constant for

$\cos\theta^* \leq 0.4$ and decreases more slowly with $\sqrt{s}$. No deep minimum is observed. The forward-backward symmetrical angular distribution for $\pi^0\gamma$ annihilations falls with increasing θ^* to a deep and broad minimum at $\cos\theta = 0.0$ and is approximately energy independent. The forward-backward symmetrical angular distribution for $\eta\pi^0$ annihilations falls to a minimum at $\cos\theta^* \sim 0.3$, rising to a secondary maximum at $\cos\theta^* = 0.0$. For $\sqrt{s} \geq 3.526$ GeV, a first minimum is observed at $\cos\theta^* = 0.45$, the secondary maximum is at $\cos\theta^* = 0.35$, and an additional minimum appears at $\cos\theta^* = 0.0$. $d\sigma/d\cos\theta^*$ for $\eta\eta$ falls to a deep broad minimum and is nearly uniform for $\cos\theta^* \leq 0.4$ with qualitatively little energy dependence of the angular distribution.

The dynamics of these reactions thus differ substantially. For $\pi^0\pi^0$ the growth of a deep minimum in the large angle cross section for $\sqrt{s} \leq 3.097$ GeV suggests a diffractive effect. For $\eta\pi^0$ we observe the apparent onset of additional partial wave amplitude(s) as we pass from our low $\sqrt{s}$ to higher $\sqrt{s}$ regime.

In Fig. 16, we present the differential cross sections, $d\sigma/dt$ at $\cos\theta^* = 0$, against $\sqrt{s}$. For each reaction we give the best fit to the form $d\sigma/dt = Cs^{-n}$. Figures 16(a) and 16(d) include the R704 data and the lower energy data ($s \leq 2.5$ GeV) of Ref. [6]. The fits to the high statistics $\pi^0\pi^0$ data are very poor, $\chi^2/df > 30$, reflecting the departures from the simple s^{-n} dependence discussed in Ref. [15]. The fits are mediocre, $\chi^2/df > 3$, for the $\eta\pi^0$ and $\eta\eta$ channels but quite good, $\chi^2/df < 1$, for the $\pi^0\gamma$ channel, where statistical errors are large due to the subtraction of the large background from the signal. We observe from the figures that, despite poor fits, the fitted lines qualitatively describe the energy dependence of the data reasonably well. Comparing the fits to the E760 data to the predictions of the models, we find $s^{-7.18\pm0.05}$ for reaction (1) compared to the $s^{-8}(s^{-7.7})$ prediction of the dimensional counting (modified Landshoff) model. For reactions (2) and (3) we obtain best fits of $s^{-14.1\pm0.1}$ and $s^{-10.7\pm0.2}$ compared to the predictions of both models of approximately s^{-8}. For reaction (4) we measure $s^{-7.2\pm0.7}$ compared to the dimensional scaling prediction of s^{-7}. We observe that reactions (1) and (4) are in fair agreement with the power-law predictions while for reactions (2) and (3), those containing ηs, the differential cross sections fall much faster with s than predicted.

In Fig. 17, we give $s^n d\sigma/dt$ at $\cos\theta^* = 0$ against $\ln s$ where we factor out the best fit s^{-n} dependence. While the scaled differential cross sections are not energy independent, we cannot clearly identify the predicted oscillations. However, the world's data spans little more than one cycle of the expected oscillation ($\lambda_{\rm lns} \sim 1$). Further discussion of models for the large angle differential cross section is found in Ref. [32].

Significant departures from s^{-n} dependence of the large angle differential cross section may be expected in our energy regime, due to interferences, the possible appearance of resonances, and our relatively small s and t. We observe that the dimensional-counting predictions hold better for reactions containing pions and γ's than for those containing η's. As may be expected from the asymptotic assumptions of that model, the modest s and t are less critical for reactions with lighter final state hadrons. Data at higher energies would be valuable to further explore this trend. Unfortunately the reach of the Fermilab Antiproton Accumulator is limited to $\sqrt{s} \leq 4.3$ GeV.

V. CONCLUSIONS

We have measured differential cross sections for $\overline{p}p \to \pi^0\pi^0$, $\eta\pi^0$, $\eta\eta$, $\pi^0\gamma$, and $\gamma\gamma$ at center-of-mass energies in the range $2.911 \leq \sqrt{s} \leq 4.274$ GeV, in the angular range $|\cos\theta^*| \leq 0.5-0.6$, where the upper value depends on reaction and energy. The large angle differential cross sections $d\sigma/dt$ for the $\pi^0\pi^0$ and $\pi^0\gamma$ channels approximately follow the s^{-n} dependence predicted by parton models with the correct values for n. However, while the $\eta\pi^0$ and $\eta\eta$ differential cross sections show a s^{-n} dependence, the powers n are significantly larger than predicted. Our data are too low in energy and too sparse to demonstrate the oscillation predicted from the interference of short-distance and Landshoff amplitudes.

ACKNOWLEDGMENTS

The authors wish to acknowledge the help of the members of the Fermilab Accelerator division. We also wish to thank the staff, engineers, and technicians at our respective institutions for their help and cooperation. This research was supported by the U. S. Department of Energy, the U. S. National Science Foundation, and the Istituto Nazionale di Fisica Nucleare of Italy.

[1] C. Baglin *et al.*, Nucl. Phys. **B368**, 175 (1992).
[2] I. S. Shapiro, Phys. Rep. **35**, 129 (1978); W. Buck *et al.*, Ann. Phys. (N.Y.) **121**, 70 (1979); R. L. Jaffe, Phys. Rev. D **17**, 1444 (1978); P. M. Fishbane and S. Meshkov, Comments Nucl. Part. Phys. **13**, 325 (1984).
[3] E. Eisenhandler *et al.*, Nucl. Phys. **B96**, 109 (1975).
[4] A. Hasan *et al.*, Nucl. Phys. **B378**, 3 (1992).
[5] A. A. Carter *et al.*, Nucl. Phys. **B127**, 202 (1977).
[6] R. S. Dulude *et al.*, Phys. Lett. **79B**, 329 (1978).
[7] A. A. Carter *et al.*, Phys. Lett. **67B**, 117 (1977); **67B**, 122 (1977).
[8] R. S. Dulude *et al.*, Phys. Lett. **79B**, 335 (1978).
[9] A. D. Martin and M. R. Pennington, Nucl. Phys. **B169**, 216 (1980).
[10] S. Takeuchi *et al.*, Nucl. Phys. **A556**, 601 (1993).
[11] S. J. Brodsky and G. R. Farrar, Phys. Rev. Lett. **31**, 1153 (1973).
[12] D. Sivers, S. Brodsky, and R. Blankenbecler, Phys. Rep., Phys. Lett. **23C**, 1 (1976).
[13] P. V. Landshoff, Phys. Rev. D **10**, 1024 (1974).
[14] A. H. Mueller, Phys. Rep. **73**, 237 (1981).
[15] C. E. Carlson, M. Chachkunashvili, and F. Myhrer, Phys. Rev. D **46**, 2891 (1992).
[16] B. Pire and J. Ralston, Phys. Lett. **117B**, 233 (1982).

[17] T. A. Armstrong *et al.*, Phys. Rev. D **52**, 4839 (1995).
[18] M. Artuso *et al.*, Phys. Rev. D **50**, 5484 (1994).
[19] T. A. Armstrong *et al.*, Phys. Rev. D **47**, 772 (1993); Nucl. Phys. **B373**, 35 (1992).
[20] M. Macri, in *Proceeding of the 1983 CERN First Accelerator School: Antiprotons for Colliding Beam Facilities*, Geneva, Switzerland, 1983, edited by P. Bryant and S. Newman, CERN Report No. 84-15, Geneva, 1984 (unpublished), p. 469.
[21] S. Trokenheim *et al.*, Nucl. Instrum. Methods Phys. Res. A **355**, 308 (1995).
[22] C. Biino *et al.*, Nucl. Instrum. Methods Phys. Res. A **317**, 135 (1992).
[23] M. A. Hasan *et al.*, Nucl. Instrum. Methods Phys. Res. A **295**, 73 (1990).
[24] L. Bartoszek *et al.*, Nucl. Instrum. Methods Phys. Res. A **301**, 47 (1991).
[25] J. E. Fast, Doctoral dissertation, University of California, Irvine, 1992.
[26] K. E. Gollwitzer, Doctoral dissertation, University of California, Irvine, 1993.
[27] O. I. Dahl, T. B. Day, and F. T. Solmitz, SQUAW: *Kinematic Fitting Program*, University of California Lawrence Radiation Laboratory Report No. P-126, 1965 (unpublished).
[28] M. Masuzawa, Doctoral dissertation, Northwestern University, 1993.
[29] T. A. Armstrong *et al.*, Phys. Lett. B **307**, 394 (1993); **37**, 399 (1993).
[30] J. J. Zhao, Doctoral dissertation, Northwestern University, 1993.
[31] T. A. Armstrong *et al.*, Phys. Rev. Lett. **70**, 2988 (1993).
[32] J. D. Reid, Doctoral dissertation, The Pennsylvania State University, 1993.